Valid time shifting Ensemble Kalman filter (VTS-EnKF) for dust storm forecasting

Mijie Pang[1], Jianbing Jin[1], Arjo Segers[2], Huiya Jiang[3], Wei Han[4], Batjargal Buyantogtokh[5], Ji Xia[1], Li Fang[1], Jiandong Li[1], Hai Xiang Lin[6,7], and Hong Liao[1]

[1]Joint International Research Laboratory of Climate and Environment Change, Jiangsu Key Laboratory of Atmospheric Environment Monitoring and Pollution Control, Jiangsu Collaborative Innovation Center of Atmospheric Environment and Equipment Technology, School of Environmental Science and Engineering, Nanjing University of Information Science and Technology, Nanjing, Jiangsu, China
[2]TNO, Department of Climate, Air and Sustainability, The Netherlands
[3]College of Environment and Resources, Nanjing Agricultural University
[4]Numerical Weather Prediction Center, Chinese Meteorological Administration, Beijing, China
[5]Information and Research Institute of Meteorology, Hydrology and Environment, Ulaanbaatar, Mongolia
[6]Delft Institute of Applied Mathematics, Delft University of Technology, Delft, The Netherlands
[7]Institute of Environment Sciences, Leiden University, The Netherlands

Correspondence: Jianbing Jin (jianbing.jin@nuist.edu.cn)

Abstract. Dust storms pose significant threats to human health and property. Accurate forecasting is crucial for taking precautionary measures. Dust models have suffered from uncertainties from emission and transport factors. Data assimilation can correct model bias by incorporating available observations, leading to improved analyses and forecasts. The Ensemble Kalman Filter (EnKF) is a widely-used assimilation algorithm that effectively tunes models, particularly in terms of intensity adjustment. However, when the position of the simulation does not align consistently with the observations which is referred to as position error, the EnKF algorithm struggles. This is because when the position error is adequately large, EnKF can hardly represent this uncertainty. EnKF can be biased for the non-Gaussian statistics. In this paper, we proposed an VTS-EnKF assimilation methodology, in which the standard EnKF is coupled with a valid time shifting method. In addition to the original ensembles quantifying dust loading variation, this methodology introduces extra ensembles from neighboring time for describing the potential spread of dust position. The enlarged ensemble captures both intensity and positional errors, allowing observations to be thoroughly resolved into the assimilation calculations. We tested the VTS-EnKF on two super dust storm events that occurred in spring 2021. The results show that position error significantly degraded dust forecasting in terms of RMSE and NMB, and hindered the EnKF from assimilating valid observations. In contrast, the VTS-EnKF yielded substantial improvements in both dust analysis fields and forecasts compared to the EnKF.

1 Introduction

Dust storms are a natural meteorological disaster (Zhang et al., 2005), whose occurrence is attributed to frequent strong winds over dry and loose soil texture (An et al., 2018). Dust particles can be lifted up to a few miles and transported over thousands of kilometers away (Zhang et al., 2018), with dust aerosol concentrations as high as thousands of $\mu g\ m^{-3}$ (She et al., 2018).

Meanwhile, these aerosols can interact with SOx and NOx undergoing heterogeneous chemical reactions during transportation, leading to further severe aerosol pollution (Song et al., 2022). These pose a great threat to human health by causing damage to the respiratory and circulatory systems (Gross et al., 2018; Goudie, 2014). East Asia, as one of the major dust sources and affected regions (Hu et al., 2019), has drawn much attention from researchers. For instance, in the 2021 spring, several super dust storms, which are recorded as the largest ones in terms of intensity and coverage in a decade (Filonchyk and Peterson, 2022), swept over East Asia and caused huge loss of lives and properties both in Mongolia and China (Gui et al., 2022; Jin et al., 2022; Tang et al., 2022). An accurate early warning of dust storms is, therefore, in essential need to help minimize the damages.

The growing interest in dust storms from the public has stimulated the understanding of the physical processes associated with the dust cycles over the past decades. To achieve the simulation of dust storms, several dust emission parameterization schemes have been proposed since the early 1990s, e.g., MB95 (Marticorena and Bergametti, 1995), Shao96 (Shao et al., 1996; Shao, 2004), Zender03 (Zender et al., 2003), and K14 (Kok et al., 2014). Coupled with chemical transport models, dust simulations could then be carried out, e.g., CUACE/DUST (Chinese Unified Atmospheric Chemistry Environment for Dust) (Gong and Zhang, 2008), BSC-DREAM8b (Dust Regional Atmospheric Modeling) (Pérez et al., 2006; Mona et al., 2014), GEOS-Chem (Duncan Fairlie et al., 2007), and LOTOS-EUROS (Timmermans et al., 2017; Manders et al., 2017). These dust models help evaluate health effects, quantify Earth system impacts, and reveal the synoptic climatic driving forces, and also to build dust early warning systems via reporting the dust loading in the few hours to few days. However, various numerical approximations are used to solve the dynamic dust equations, so that the model configuration (like coarse grid cell and time step), uncertain input data (e.g., wind field and boundary/initial conditions) inevitably limit the model forecast skill (Mallet and Sportisse, 2006). Notably, it is widely accepted that uncertainty in the emission parameterization is the largest error source of dust simulation (Ginoux et al., 2001, 2012; Di Tomaso et al., 2017, 2022; Jin et al., 2019a, b). The performance of numerical dust models degrades greatly due to these factors.

Observation is another fundamental method for exploring the intensity and spatial distribution of dust storms (Muhammad Akhlaq et al., 2012). Satellite-based observations are a rapidly developing technology that is widely used in detecting dust storms (Gui et al., 2022). Products from satellites such as MODIS, Himawari, and Fengyun-4A provide various information about aerosol properties with high spatial resolution and extensive coverage. However, they only retrieve column-cumulative values and are easily affected by clouds and other particles. Therefore, significant uncertainties and biases exist, and pre-processing is necessary before they can accurately represent dust load (Jin et al., 2019b, 2022). Ground-based observation networks, on the other hand, are highly reliable and have high temporal resolution, making them indispensable for measuring dust aerosol concentration (She et al., 2018). In recent years, China has invested heavily in the construction of a ground station network, and there are now over 1600 ground stations throughout China that provide a comprehensive picture of dust plumes (Gui et al., 2022). The national observation network provides rich measurements for investigating dust storms in East Asia.

Data assimilation is a powerful technique that integrates models and observations. Based on Bayesian theory, data assimilation algorithm is intended to calculate the posteriori probability distribution of the model state given the observations as accurately as possible (Law and Stuart, 2012). Two main approaches to data assimilation are variational methods and filtering

methods. Variational methods, such as 4DVar, aim to retrieve an optimal posterior analysis that fits both the prior and measurements over a time window by minimizing a cost function (Rabier and Liu, 2003). Variational methods are widely used in inverse modeling of initial conditions and emission fields (Jin et al., 2022; Bergamaschi et al., 2010; Corazza et al., 2011) and reanalysis data, but they require tangent linearization or adjoint of the model, which can be challenging to develop and maintain. The cost function minimization is computationally demanding, especially for high-dimensional and nonlinear models. Filtering methods, on the other hand, assimilate observations sequentially and are more efficient for operational forecasting systems. Various filtering approaches, such as Kalman Filter (Kalman, 1960), Extended Kalman Filter (Brunner et al., 2012), and Particle Filter (Leeuwen et al., 2019), have been developed. Among all the filtering methods, the Ensemble Kalman Filter (EnKF) is the most popular filtering method due to its ability to handle high-dimensional models, easy parallelization (Evensen, 1994; Katzfuss et al., 2016; Houtekamer and Zhang, 2016). It uses limited ensembles to estimate the background error covariance statistics of the model (Hamill, 2006; Houtekamer et al., 2014). Its advantages include handling non-linearity, not requiring explicit calculation of tangent linear operators, and computational efficiency (Bannister, 2017). EnKF has been successfully applied in various disciplines, e.g.,weather forecasting (Houtekamer et al., 2005) and hydrology (Reichle et al., 2002). Meanwhile, inherited from Kalman filter, EnKF relies on Gaussian distribution of error statistics (Amezcua and Van Leeuwen, 2014). For non-Gaussian problems, EnKF can create suboptimal results (Lei et al., 2010).

The primary source of uncertainty in dust simulation is related to the online emission parameterization. Therefore, most previous studies on dust storm data assimilation have focused on emission inversion. For example, Yumimoto and Takemura (2015) used MODIS AOD retrievals for long-term dust emission inverse modeling over Asia. Escribano et al. (2017) investigated the impact of five different satellite AOD products on dust emission inversion over northern Africa and the Arabian Peninsula. Their results indicated that the assimilation outcome is more sensitive to model uncertainties than to observational uncertainties in some cases. The uncertainties in model actually have a greater impact in the assimilation results. In recent studies, we have carefully explored the variability of dust emission over the Mongolia and China Gobi desert by assimilating ground-based PM_{10} concentration (Jin et al., 2018), polar-orbiting MODIS (Jin et al., 2022), and geostationary Himawari-8 AOD measurements (Jin et al., 2019b). To effectively improve dust storm emission inversion, we introduced observation bias correction (Jin et al., 2019a), adjoint-based emission source tracking (Jin et al., 2020), and grid distortion (Jin et al., 2021). These works provide valuable insights into the dynamics of dust emission and quantify their impacts on the environment and climate. However, little attention has been paid to the application of high-quality dust storm sequential forecasting using filter methods. Recently, we have developed a data assimilation-based operational dust forecasting system by coupling Ensemble Kalman Filter (EnKF) and Localized Ensemble Kalman Filter (LEnKF) assimilation algorithms with a chemical transport model (LOTOS-EUROS) through an interface of our self-designed assimilation toolbox, Pyfilter (Pang, last access: Nov. 2023). We tested this system on the super dust storms that occurred in the spring of 2021, as we will show later. Significant improvements were found in the assimilation analysis and assimilation-based forecasts compared to the pure model results. Furthermore, the LEnKF algorithm with a proper localization distance threshold was consistently shown to be superior to the EnKF algorithm.

Despite the positive results obtained from our tests, there are still unresolved errors. One major issue is the apparent mismatch between the observations and model in space after long-distance transport. In addition to the discrepancy in the dust intensity, as will be illustrated in Sect. 2.4, the timing of the dust arrival and departure reported by the model simulation also differs heterogeneously from reality. The dust intensity is a key feature, as well as the position, when evaluating a dust forecast. The former represents the actual dust load, while the latter reveals where the dust plume affects at a given instant. For an operational forecasting and warning system, the position information is sometimes more important than the intensity. In terms of mathematical metrics, such as root mean square error, the forecasting skills degraded significantly with the presence of the position mismatch. The detailed mechanism behind this issue and its further consequences will be illustrated in Section 3.2.

The so-called "position error" in dust aerosol simulations typically arises after long-distance transport. There are many factors that contribute to the position error, such as simplified physical processes, coarse model resolution, uncertain physical parameters (Ravela et al., 2007), and the uncertainty in the meteorological field and emission timing, as illustrated in our previous work (Jin et al., 2021). Similar to the dust emission inversion studies discussed above, the deviations between the model and observations in dust storm data assimilation are also attributed to the uncertainty in the dust emission, where ensemble individuals are generated with perturbed dust emission fields. However, the uncertainty in the dust plume position is difficult to quantify and is hardly taken into account when designing the background error covariance of the simulated dust plume. Therefore, classic dust data assimilation methodologies now focus on intensity adjustment and are not capable of handling the imbalanced uncertainties between the observations and simulation caused by the position error.

Position error is not a mere occasional issue, but rather a cumulative error that accompanies model simulations over time. This type of error is quite common in forecasting phenomena such as hurricanes, dust storms, thunderstorms, and precipitation (Dance, 2004; Nehrkorn et al., 2015; Jin et al., 2021). However, there have been relatively few studies aiming to address this problem. Brewster (2003) proposed an objective method for identifying and correcting position errors using densely-distributed and high-resolution observational data. Their research demonstrated that it is possible to correct position errors in Observing System Simulation Experiments (OSSEs). Jin et al. (2021) developed a grid-distortion technique based on image morphing and post-processing, which successfully realigned dust plumes to better match the measurements. Both of these improvements rely on densely distributed observations, but often the observations do not fully cover the entire domain, limiting the applicability of these methods.

In this paper, the standard EnKF assimilation is coupled with a valid time shifting (VTS) method (Xu et al., 2008; Lu et al., 2011; Zhao et al., 2015; Huang and Wang, 2018) for better resolving the position error in long-distance dust storm transport simulation. This assimilation methodology is referred to as VTS-EnKF throughout this paper. For assimilation analysis at a given time, the background error covariance of the simulated dust plume is calculated using not only the original ensemble simulation, but also the same ensemble simulations at neighboring moments (a few hours earlier and later) (Gasperoni et al., 2022, 2023). These extra ensemble members represent the potential position spread of the actual dust plume, effectively accounting for transport errors. The resampled ensemble members quantify the complex covariance that captures both intensity and position error dynamics, without requiring additional processing on observations, meteorological fields, or other physical parameters. We tested the VTS-EnKF on two severe dust storm events that occurred in 2021. Our results show superior

assimilation performance compared to the standard EnKF, particularly when position errors are present in the simulated dust plume.

This paper is organized as follows: Section 2 introduces the dust measurements and dust model used in the research. We also discuss that the major uncertainty of dust model forecast comes from the emission. But there is another problem: position error that remains to be solved. Then in Sect. 3, we explain introducing the procedure of ensemble-based assimilation algorithm and the mechanism of position error's negative effect on EnKF. How the new assimilation method works is explained in detail afterwards. To test the performance of EnKF with VTS, sequential assimilation experiments on several dust storm events are designed. Section 4 analyses the results of experiments in terms of both the assimilation analysis and forecast performance. Section 5 concludes this paper.

2 Dust measurement, model and position error

In this paper, ground-based PM_{10} is used as the measurement with a bias-correction procedure to remove the non-dust part. The dust model adopted is the LOTOS-EUROS. Considering the model processes, the greatest uncertainty in the dust simulation comes from uncertainty the emission parameterization. Meanwhile, uncertainties from meteorology can also influence the model forecast and lead to the "Position error".

2.1 Dust measurements

Thanks to the continuous efforts and investments from the Ministry of Ecology and Environment, over 1600 ground monitoring stations have been established across China, with some locations in northern China shown in Fig. 1. These stations provide real-time hourly air quality data, and their hourly PM_{10} concentrations serve as indispensable datasets for measuring dust load, which are used as observations in this paper.

Despite the advantages of low uncertainty and high time resolution, PM_{10} observations are not assimilated directly due to the mixed state of dust and non-dust aerosols in the original PM_{10} data. Anthropogenic activities, such as vehicle emissions, coal burning, and industrial processes (Wu et al., 2018; Liu et al., 2018), along with natural sources like volcanic eruptions, sea spray, wildfires, and wind-blown dust contribute to the total PM_{10} concentration. Assimilating PM_{10} data directly into a dust model may introduce biased errors and lead to model divergence (Jin et al., 2019a). Therefore, it is necessary to eliminate the bias before data assimilation.

In this study, the non-dust portion of PM_{10} is approximated through a separate model. The dust observations assimilated are calculated by subtracting the non-dust fraction from the original PM_{10} measurements. Further details regarding the baseline removal (BR) can be found in Jin et al. (2022).

2.2 Dust model

In this paper, the LOTOS-EUROS v2.1 is used to simulate dust storms that occurred in East Asia. Originating from the Long-Term Ozone Simulation (LOTOS) and the European Operational Smog model (EUROS) in the 1980s, LOTOS-EUROS has

undergone continuous development for various applications. It has been widely used in air quality forecasting (Curier et al., 2012; Brasseur et al., 2019; Lopez-Restrepo et al., 2020; Skoulidou et al., 2021), dust/aerosol emission inversion (Yarce Botero et al., 2021; Jin et al., 2018, 2019a, b, 2021, 2022), and source apportionment (Kranenburg et al., 2013; Timmermans et al., 2017; Pommier et al., 2020; Jin et al., 2020). In spring 2021, several super dust storm events occurred in East Asia, around 15th March, 28th March. These events, referred to as DSE1 and DSE2, are used as test cases in this study. These dust storms caused significant losses in both Mongolia and China (Jin, 2021; Chen and Walsh, 2021). Accurate forecast of such severe sandstorms is crucial for reducing health and property damages.

To simulate the dust storm over East Asia, LOTOS-EUROS is configured following our recent work (Jin et al., 2022): The simulation domain is from $15°$ N to $50°$ N and $70°$ E to $140°$ E with a grid resolution of $0.25° \times 0.25°$. The model consists of 8 layers with a top at 10 km. The boundary conditions are set to zero assuming that all the dust aerosols are emitted during the simulation window. Dust emission, deposition, advection, diffusion and dry/wet deposition are considered within the model. The model output is at the interval of 1 hour.

The whole model simulation period is set from 13 to 17 March for DSE1 and 27 to 30 March for DSE2, which covering the whole life cycles of emission and long-distance transport. More details could be found in Jin et al. (2022).

2.3 Uncertainties from emission and meteorology

The goal of this study is to calculate the dust concentration field that best fits both the a priori and observations at each assimilation analysis. The optimized field will then be used as the initial condition for sequential dust forecasts, as explained in Section 3.1. It is essential to define and quantify the uncertainty in dust simulations. As previously mentioned, the uncertainty in emission parameterization is widely believed to be the dominant error source in dust simulation (Ginoux et al., 2001, 2012; Di Tomaso et al., 2017, 2022; Jin et al., 2019a, b). High levels of uncertainty in dust emission parameterization arise from insufficient knowledge about windblown erosion, lack of accurate input on soil characteristics, and the models' inability to resolve the fine-scale variability in wind fields governing dust emission (Escribano et al., 2017; Foroutan et al., 2017; Foroutan and Pleim, 2017; Jin et al., 2019b).

In our recent work (Jin et al., 2022), a 4DVar-based inverse modeling approach was employed to retrieve an optimal emission field for the three major dust storms in spring 2021 (Jin et al., 2022). The a priori emission, $\boldsymbol{f}_{\text{priori}}$, followed the *Zender03* dust emission parameterization scheme (Zender et al., 2003). To compensate for potential errors, a spatially varying multiplication factor was introduced. Mathematically, it was quantified by a background error covariance matrix, $\mathbf{B}$, to describe the potential spread of the actual dust emission flux.

Another source of the uncertainties arises from the meteorological field. In our previous papers, uncertainties from meteorology and the position error were neither taken into account (Jin et al., 2022; Pang et al., 2023). In this paper, European Center for Medium-ranged Weather Forecast (ECMWF) ensemble forecast (totally 51 ensembles) are used. Each one of the model ensembles is driven by one unique ensemble meteorology field. N=32 ensemble meteorological fields are randomly selected. Its grid resolution is about 14 km. The 6-hourly short-term meteorological forecast field is interpolated to hourly values. The grid resolutions are also averaged to fit the model resolution.

In general, we assign the dust simulation uncertainty to both emission and meteorology. Ensemble emission field $[\boldsymbol{f}_1, ..., \boldsymbol{f}_{\mathrm{N}}]$ are generated randomly following the emission uncertainty choice $\boldsymbol{f}_{\mathrm{priori}}$ and $\mathbf{B}$ in Jin et al. (2022). Meteorologic field $[\boldsymbol{w}_1, ..., \boldsymbol{w}_{\mathrm{N}}]$ are randomly selected from the total 51 ensemble meteorology. They are used to forward the LOTOS-EUROS model $\mathcal{M}$ for the ensemble dust simulations $[\boldsymbol{x}_1, ..., \boldsymbol{x}_{\mathrm{N}}]$ as:

$$[\boldsymbol{x}_1, \ ... \ , \boldsymbol{x}_{\mathrm{N}}] \ = \ [\mathcal{M}(\boldsymbol{f}_1, \boldsymbol{w}_1), \ ... \ , \ \mathcal{M}(\boldsymbol{f}_{\mathrm{N}}, \boldsymbol{w}_{\mathrm{N}})] \tag{1}$$

N refers to the total ensemble number, and the choice will be explained in Section 3.3.

These ensemble individuals are used in the EnKF assimilation for representing the covariance dynamics of the dust plume, which resulted in more accurate dust analysis and forecast as will be shown in Sect. 4. However, the ensemble realizations mainly represent the uncertainty in the intensity feature, and hardly help resolve the positional deviation between the observation and simulation. The presence of position error would give rise to a divergent assimilation analysis as will be illustrated in Sect. 3.1.

2.4 Position error

For all the dust events, most of the dust particles were originated from the Mongolia Gobi desert, and carried by the prevailing wind towards southeast. After several thousands of kilometers transport which lasted about one to two days, they finally arrived in the densely-populated northern China.

Position errors are clearly visible in the simulation of two dust events (DSE1 and DSE2). Examples can be best seen in Fig. 1, which plots the evolution of LOTOS-EUROS simulated surface dust concentration alongside BR-PM_{10} (BR: non-dust baseline-removed) concentration observations for DSE1 (panel a) and DSE2 (panel c). The corresponding standard deviations from ensemble model simulations and the model-minus-observation differences (absolute values) are also plotted in panel b and panel d. In panel a.1, the model generally simulates a similar shape of the dust plume as indicated by the observations at the first instance, though the dust load intensities differ to some extent. However, during the subsequent transport, positional errors arise gradually. In panel a.2, the right part of the simulated dust plume is positioned about 100 to 200 km too far south compared to ground-based observations. Consequently, the Root Mean Square Error (RMSE) increases significantly from 587.83 $\mu g\ m^{-3}$ at 8:00 to 856.36 $\mu g\ m^{-3}$ at 11:00. This position error continues to accumulate over the following 3 hours at 14:00. The development of position errors is further clearly visible against the PM_{10} observations, especially in the light blue box in panel a.3. The model simulation missed all the dust load there, while the observations indicate a significant amount of dust aerosols. It can also be seen in panel b.3 that the model-minus-observation differences exceed 1000 $\mu g\ m^{-3}$ there. Similarly, for DSE2 occurring on 28th March, 2021, as shown in Fig. 1(c), discrepancies between observations and simulation become more explicit as time evolves, especially for the dust in the light blue box in panels c.1 and c.2. The RMSE remains high from 542.15 $\mu g\ m^{-3}$ at 8:00 to 479.6 $\mu g\ m^{-3}$ at 11:00, and this error expands to a wider extent as shown in the enlarged green box in panel c.3. This position error not only limits the pure model forecast performance but also significantly degrades the subsequent assimilation analysis and forecast. With an ensemble-approximated background covariance unrepresentative of position error, neither the position deviation nor the intensity deviation can be fully resolved, as will be explained in Sect. 3.2.

Potential sources of position error in dust model may be attributed to inaccuracies in emission timing, uncertainties in meteorological input data (e.g., wind fields responsible for transporting dust plumes from the Gobi Desert in Mongolia and China to downwind regions), or a combination of these factors. Adjusting the emission timing profile, which characterizes the release of soil particles into the atmosphere, could partially correct the position of the dust plume. Moreover, alterations in meteorological conditions governing long-distance transport might also realign the dust plume's position. To address the position error, a comprehensive covariance matrix is necessary to account for both the potential variations in emission temporal profiles and the accumulation of uncertainties along the plume's extensive trajectory. Concurrently, a significantly larger ensemble size is required to propagate these uncertainties, featuring high degrees of freedom, into the PM_{10} observational space. Although a sophisticated covariance matrix and a substantial ensemble size (resulting in considerable computational cost) may aid the EnKF in simultaneously resolving position and intensity errors, this approach is often prohibitively expensive. Therefore, an efficient and cost-effective alternative solution is required.

3 Assimilation methodology and experiments

EnKF is a powerful algorithm to tune the model simulation with observations especially in intensity adjustment given the perturbed emission spreads. However, when faced with the position error, its weakness is exposed that some model-minus-observation inconsistency cannot be resolved by EnKF as illustrated in Section 3.1. On the contrary, our EnKF with VTS can correct both the position error and the intensity. Assimilation strategy is designed and embeded into a assimilation forecast system in Section 3.2. Experiments are designed on the dust storms occur in spring, 2021, which are illutrated in Section 3.3.

3.1 EnKF

The Ensemble Kalman Filter (EnKF) was first proposed by Evensen (1994). Stemming from the Kalman Filter, it was designed to address high-dimensional problems by employing limited ensembles to approximate the true background error covariance. It relies on the Gaussian distribution of errors. The EnKF has been proven to be practical and efficient in various applications, particularly in sequential forecasting with the aid of localization (Lopez-Restrepo et al., 2020; Park et al., 2022). In any sequential forecast system, the objective of assimilation analysis is to provide an optimized initial state or parameter field, which, in this study, corresponds to the 3D dust concentration. This is achieved by assimilating the available measurements. The estimated dust concentration field can then be used to onward the model for more accurate dust forecasting.

Here we use the stochastic EnKF formulated by Burgers et al. (1998). It features the pertubated observations to maintain a reliable ensemble spread. Starting from the prior dust concentration field $\boldsymbol{x}_t^{f,i}$ at time t which is calculated by model integral operator $\mathcal{M}$ from the dust concentration field at the previous time step $\boldsymbol{x}_{t-1}^{a,i}$.

$$\boldsymbol{x}_t^{f,i} = \mathcal{M}(\boldsymbol{x}_{t-1}^{a,i}, \boldsymbol{f}^i, \boldsymbol{w}^i) \tag{2}$$

$$\mathbf{X}^f = [\boldsymbol{x}_t^{f,1}, \boldsymbol{x}_t^{f,2}, \cdots, \boldsymbol{x}_t^{f,\mathrm{N}}] \tag{3}$$

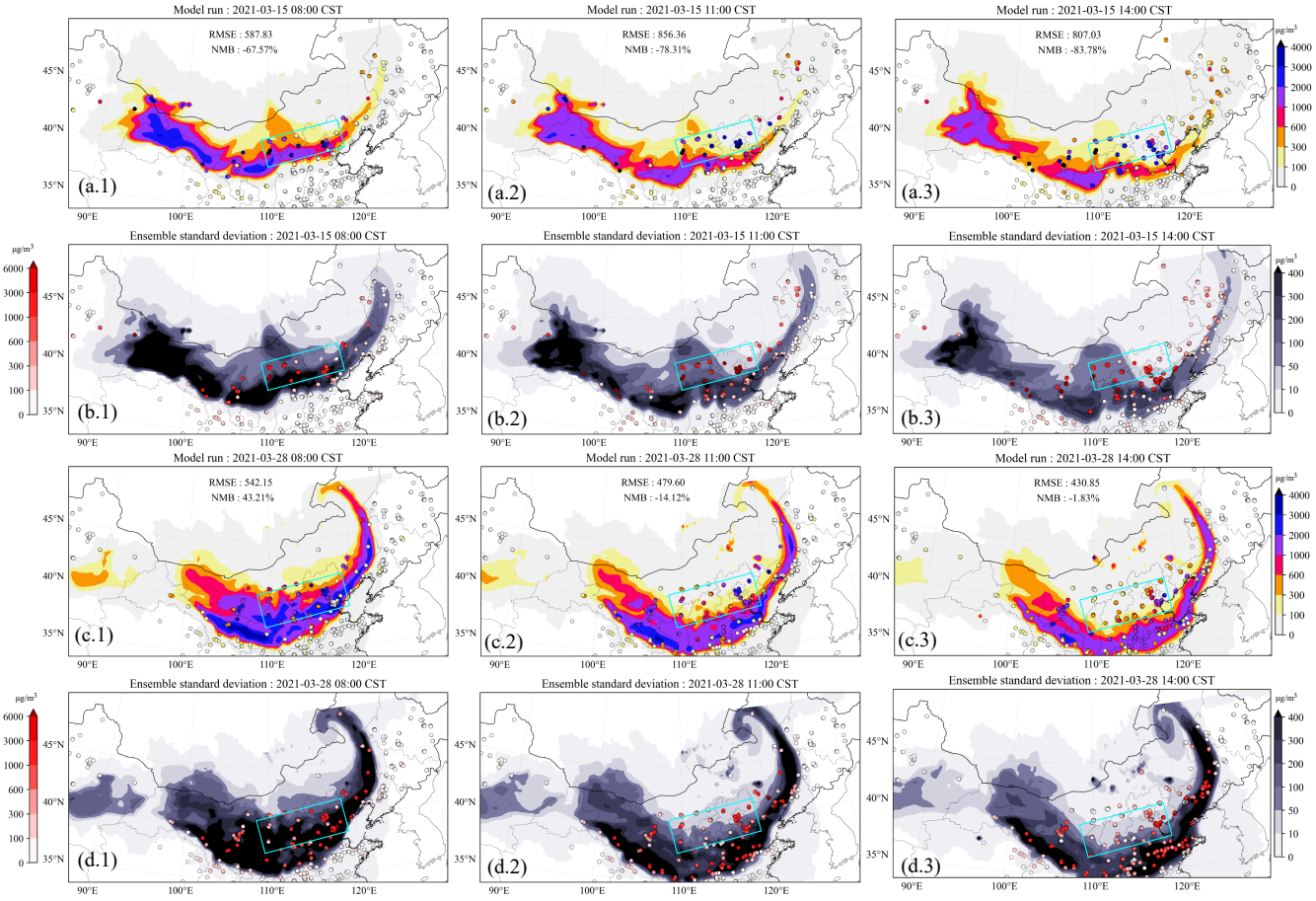

Figure 1. Evolution of the simulated dust plume from average of 32 model ensembles with scatter of ground BR-PM_{10} observations (**a.1-3**). Their corresponding standard deviation from model ensembles with scatter of the model-minus-observation differences (absolute value) (**b.1-3**) at 08:00, 11:00 and 14:00 15th March, 2021, respectively. Figures below are the same except the time is at 05:00 (**c.1** and **d.1**), 08:00 (**c.2** and **d.2**), 11:00 (**c.3** and **d.3**) 28th March, 2021, respectively. BR-PM_{10}: baseline-removed PM_{10}. The colorbar in panel **a** and **c** represents the concentrations, and the colorbar in panel **b** and **d** represents the model-minus-observation differences (left) and standard deviation (right).

Note that for the first analysis the prior dust simulation are extracted from the model with the perturbed emissions as shown in Eq. 1. The i represents the ensemble individual number. N is the number of ensembles. $\mathbf{X}^f$ is the ensemble model simulation matrix consists of the whole ensemble individuals.

The ensemble perturbation matrix $\mathbf{X}^{f\prime}$ calculates the deviation between the ensemble individuals $\boldsymbol{x}_t^{f,i}$ and the ensemble mean state $\overline{\boldsymbol{x}}_t^f$.

$$\overline{\boldsymbol{x}}_t^f = \frac{1}{\mathrm{N}} \sum_{i=1}^{\mathrm{N}} \boldsymbol{x}_t^{f,i} \tag{4}$$

$$\mathbf{X}^{f\prime} = [\boldsymbol{x}_t^{f,1} - \overline{\boldsymbol{x}}_t^f, \boldsymbol{x}_t^{f,2} - \overline{\boldsymbol{x}}_t^f, \cdots, \boldsymbol{x}_t^{f,\mathrm{N}} - \overline{\boldsymbol{x}}_t^f] \tag{5}$$

Then the background error covariance matrix $\mathbf{P}^f$ is approximated by $\mathbf{X}^{f\prime}$ as follows:

$$\mathbf{P}^f = \frac{1}{\mathrm{N}-1} \mathbf{X}^{f\prime} \mathbf{X}^{f\prime\,\mathrm{T}} \tag{6}$$

Afterwards, the Kalman gain $\mathbf{K}$ can be calculated with $\mathbf{P}^f$ and $\mathbf{O}$.

$$\mathbf{K} = \mathbf{P}^f \boldsymbol{\mathcal{H}}^{\mathrm{T}} (\boldsymbol{\mathcal{H}} \mathbf{P}^f \boldsymbol{\mathcal{H}}^{\mathrm{T}} + \mathbf{O})^{-1} \tag{7}$$

$\mathbf{K}$ weights the increments given from the observations to the prior estimation. In this paper, they are the BR-PM_{10} observations stored in $\boldsymbol{y}$ and dust simulation stored in vector $\boldsymbol{x}$. $\boldsymbol{\mathcal{H}}$ is the observation operator which maps the model states into the observational space.

$\mathbf{O}$ is the observational error covariance matrix that weights the uncertainty of the measurements. In this case, it is the uncertainties from ground-based BR-PM_{10} concentrations. $\mathbf{O}$ is defined as follows: the minimum uncertainty threshold is set to be 200 μg m^{-3}. Root of error from observations below the threshold is set to be 200 μg m^{-3} and those over it is set to be 200+($\boldsymbol{y}$-200)×0.2 μg m^{-3}. This definition can prevent the posteriori from getting too close to the low value observations and thus leading to model divergence. $\mathbf{O}$ is a diagonal matrix assuming that all the observations are independent.

In the end, the posteriori estimation individual $\boldsymbol{x}_t^{a,i}$ can be updated as follows:

$$\boldsymbol{x}_t^{a,i} = \boldsymbol{x}_t^{f,i} + \mathbf{K}(\boldsymbol{y} + \boldsymbol{\epsilon}^i - \boldsymbol{\mathcal{H}} \boldsymbol{x}_t^{f,i}) \tag{8}$$

$\boldsymbol{\epsilon}^i$ represents the sampling error vector. It is a random vector subjecting to normal distribution. Its mean is 0 and covariance is the root of diagonal from $\mathbf{O}$.

The equations presented above describe the Ensemble Kalman Filter (EnKF) algorithm for dust storm assimilation, which focuses on intensity adjustment. The EnKF assimilation aims to compute an optimal posteriori estimation given a priori information and observations. It is highly dependent on the observations and the ensemble spread. In fact, the ensemble-based background covariance matrix, $\mathbf{P}^f$, utilizes the ensemble members to approximate the true background covariance. The spatial distribution of the standard deviation (square root of the diagonal values in $\mathbf{P}^f$) from 32 model ensembles, along with

the scatter of absolute model-minus-observation differences in two cases (DSE1, DSE2), is shown in Fig. 1 (b,d). In general, their spatial distribution corresponds well to the simulated dust field depicted in Fig. 1 (a, c). Concurrently, the uncertainty in the light blue box decreases rapidly as the simulated dust plume moves southward, as illustrated in panels b.1 and b.2. This suggests that our ensemble model simulations are highly confident that there are less affected by dust aerosols. However, the observations indicate that this area remains heavily polluted. In the case of DSE2, the situation becomes more complex. The simulated dust plume in DSE2 covers most of the observation area with a high dust load, as demonstrated in panels c.1 and d.1. The uncertainty, on the other hand, reveals that the ensemble model is less confident about the dust load, especially in the light blue box displayed in panel d.2. After 3 hours, these discrepancies become more evident. The extent to which this situation affects the EnKF assimilation will be discussed in this paper. It poses a challenge to EnKF assimilation in resolving the high-value measurements in this region.

The performance of EnKF deteriorates when position errors are present. The underlying mechanism can be best understood by examining Fig. 2(a). At time point t_0, there are ensemble model simulations (gray dashed lines) distributed across the three-dimensional space. The black line and blue star represent the average of model ensembles and observations, respectively. As clearly depicted, there is a positional mismatch between the ensemble model simulations and observations. Following the assimilation analysis, the intensity of the dust plume is adjusted to better match the observations. However, in the spatial domain outside the priori, the dust concentration is reduced to near-zero levels. The observations in this area, containing valuable information about dust load, contribute little to correcting the dust load. This is due to the unanimous agreement on the dust load from the model ensembles, which represents low uncertainty. In such cases, the assimilation analysis favors the model results and disregards the observations. Consequently, the a posteriori estimate is biased as a result of imbalanced uncertainties.

3.2 VTS-EnKF

To efficiently perform the assimilation analysis with both the intensity and position errors present, we apply a "valid time shifting" method into the EnKF. The strategy is illustrated in Fig. 2(b). Instead of using the ensemble simulations solely at the exact assimilation analysis instant t_0, as shown in panel a, ensembles at neighboring moments are also introduced to expand the ensemble group. These resampled ensembles at neighboring times represent the potential positions of the actual dust plume. The enlarged ensembles exhibit a more extensive spread of the dust plume in the spatial domain compared to those displayed in panel a. The joint ensemble model simulations then capture uncertainty in both intensity and position. The a posteriori estimate (red line) is adjusted to better fit the observations, with both of these errors resolved.

Mathematically, the EnKF with VTS procedures are very similar to those of EnKF, except that the original $\mathbf{X}^f$ is replaced by $\mathbf{X}^{f,new}$, which stores the enlarged ensemble members at the assimilation analysis instant and neighboring times. It starts with

$$\mathbf{X}^{f,new} = [\boldsymbol{x}_{t-\tau}^{f,1}, \boldsymbol{x}_{t-\tau}^{f,2}, \cdots, \boldsymbol{x}_{t-\tau}^{f,\mathrm{N}}, \boldsymbol{x}_{t}^{f,1}, \boldsymbol{x}_{t}^{f,2}, \cdots, \boldsymbol{x}_{t}^{f,\mathrm{N}}, \boldsymbol{x}_{t+\tau}^{f,1}, \boldsymbol{x}_{t+\tau}^{f,2}, \cdots, \boldsymbol{x}_{t+\tau}^{f,\mathrm{N}}] \tag{9}$$

Let t be the exact assimilation time, and τ be the time interval. Then $t-\tau$ represents the time in the past, and $t+\tau$ represents the time in the future. It is noteworthy that the time axis, denoted by $t-\tau$ and $t+\tau$, is utilized solely to illustrate the application of ensemble simulations at different time direction in the formula. However, in practical applications, ensembles from multiple adjacent time instants can be incorporated, as demonstrated in the horizon choice utilized in this study (as presented in Table 1).

Subsequently, the ensemble-based background covariance $\mathbf{P}^f$, Kalman gain $\mathbf{K}$ and posteriori state $\boldsymbol{x}^a$ will be updated with the $\mathbf{X}^{f,new}$ in Eq. 6 $\sim$ 8, respectively.

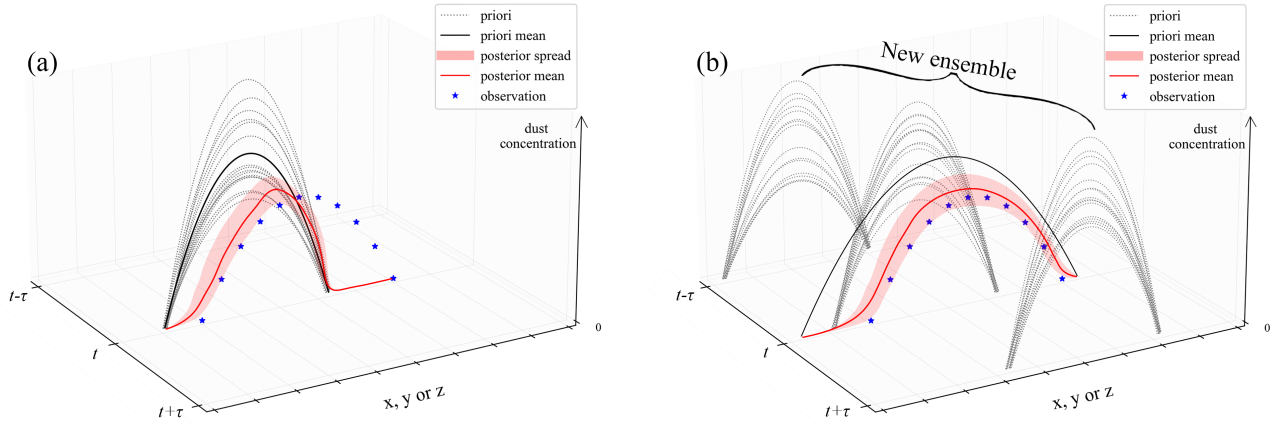

Figure 2. Strategy illustration of ensemble Kalman filter (EnKF) (**a**) and ensemble Kalman filter with VTS (VTS-EnKF) (**b**). Figure axis left represents the time and right represents the position of the dust field in 3D space. The vertical axis represents the intensity of the dust.

The localization method is also adopted here to cut off the spurious correlation in $\mathbf{P}^f$ and constrain the background covariance to a certain distance. The localization matrix is constructed following Gaspari and Cohn (1999) (Eq. A.27) with a distance threshold L_{thres}. The details about the construction of $\mathbf{L}$ can be found in Supporting Information. The localized $\mathbf{P}^{f,local}$ is obtained by point to point multiply with localization matrix $\mathbf{L}$.

$$\mathbf{P}^{f,local} = \mathbf{P}^f \circ \mathbf{L} \tag{10}$$

With the localized $\mathbf{P}^{f,local}$, the localized posteriori estimation $\boldsymbol{x}_t^{a,i}$ can be updated via Eq. 7 and Eq. 8.

Both the EnKF and EnKF with VTS described above are embeded into our self-designed assimilation toolbox, PyFilter (Pang, last access: Nov. 2023). This toolbox features a flexible interface for linking to numerical models (Pang et al., 2023), such as the dust storm forecasting model LOTOS-EUROS used in this study.

3.3 Experiment descriptions

DSE1 and DSE2 are chosen as the cases for the test. The first assimilation analysis did not commence until the dust plume was detected by the ground-based observation network and a position mismatch emerged. An identification index is also designed to objectively discriminate the position error as can be found in Eq. S3 in Supplementary. Three sequential EnKF analyses are conducted in each dust event at three-hour intervals. The timeline for DSE1 and DSE2 is depicted in Fig. 3.

Taking DSE1 as an example, the initial assimilation analysis is performed at 11:00 March 15, when an apparent position error was present, as illustrated in Fig. 1 (a.2). The last analysis is carried out at 17:00 March 15. As the dust loading decreases rapidly when the plume moves further southeast, no additional assimilation is performed. A rolling forecast (red line with arrow) is generated based on the optimized dust concentration field with a 24-hour horizon for the purpose of examining forecast skill.

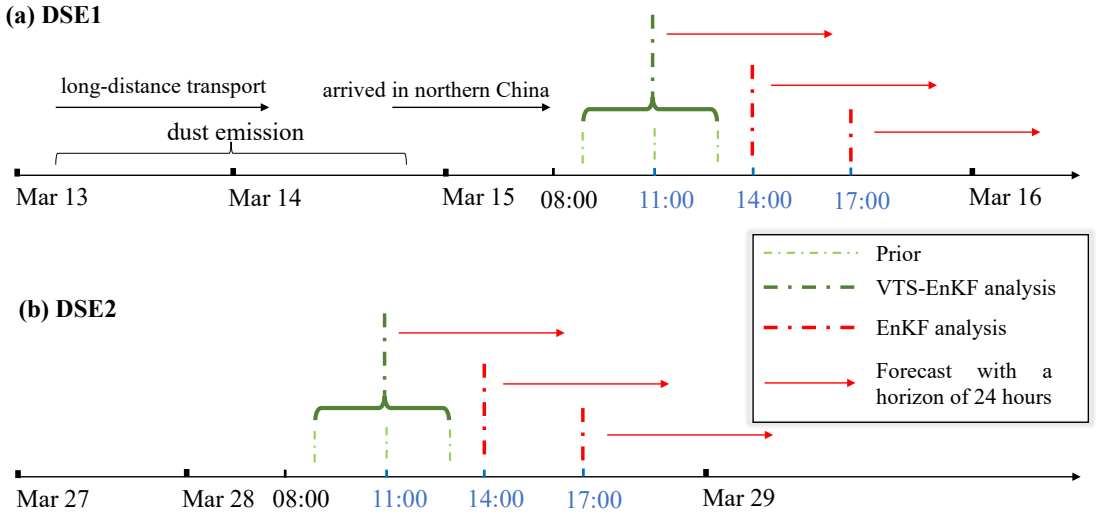

Figure 3. Sequential assimilation time set for DSE1 (**a**) and DSE2 (**b**). Take DSE1 for instance, the assimilation analysis is performed at the intervals of 3 hours from 11:00 to 17:00 and the rolling forecast is made with a horizon of 24 hours based on the assimilation analysis. The EnKF with VTS and EnKF is performed in turn.

To evaluate the performance of the VTS-EnKF-implemented dust storm forecasting system, data assimilation experiments are conducted on two spring dust events in 2021. Experiment settings are shown in Table 1. *Control* represents the ensemble model forecast throughout the entire dust storm period. *EnKF* and *L500* denote the assimilation-based forecasts by EnKF and

localized EnKF (LEnKF) with a localization distance threshold of 500 km, respectively. *VTS-EnKF* and *VTS-L500* represent the assimilation-based forecasts by VTS-EnKF and VTS-EnKF with a localization distance threshold of 500 km. Note that various distance thresholds have been tested for localization, and a choice of 500 km is found to provide the optimal assimilation analysis and forecast in our tested cases. The metrics, Root Mean Square Error (RMSE) and Normalized Mean Bias (NMB), are employed in this paper to evaluate system performance.

In EnKF-based experiments, *EnKF* and *L500*, the ensemble number N is set to 32, which is found to be sufficient to represent the uncertainty in the dust simulation while remaining computationally affordable. Testing with N greater than 32 shows only limited improvements. For VTS-EnKF experiments, the ensembles are expanded as they incorporate ensemble simulations from neighboring instants. To cover the potential positions of the dust plume, neighboring times with ±1 and ±2 hours apart are empirically chosen in this paper. As demonstrated in Table 1, the ensemble number is extended to 160 when EnKF with VTS is applied, and the neighboring time stamps of 9:00, 10:00, 12:00, and 13:00 are selected. The 160 ensemble dust simulations are updated according to the EnKF principles and forwarded synchronously for the new rolling forecast; they will serve as the prior in the subsequent assimilation analysis.

Experiments for the VTS-EnKF with equal ensembles to EnKF are designed, as referred to *VTS-EnKF-small* and *VTS-L500-small*. They starts with central 8 ensembles and are extended to 32 ensembles by incorporating neighboring ±1 and ±2 hours with 4×6 ensembles. Furthermore, to test the sensitivity of neighboring time interval, VTS-EnKF experiments with different intervals are also designed. Time intervals ranging from 1 to 5 hours are selected to test the impact, which are referred to as *VTS-EnKF-t1*, *VTS-EnKF-t2*, *VTS-EnKF-t3*, *VTS-EnKF-t4* and *VTS-EnKF-t5*.

Table 1. Experiment settings.

Name	Running ensemble number	Initial assimilation time set (hour)	Ensemble set	Localization distance (km)
Control	32	None	[32]	None
EnKF	32	t	[32]	None
L500	32	t	[32]	500
VTS-EnKF	160	$t-2, t-1, t, t+1, t+2$	[32,32,32,32,32]	None
VTS-L500	160	$t-2, t-1, t, t+1, t+2$	[32,32,32,32,32]	500
VTS-EnKF-small	32	$t-2, t-1, t, t+1, t+2$	[6,6,8,6,6]	None
VTS-L500-small	32	$t-2, t-1, t, t+1, t+2$	[6,6,8,6,6]	500
VTS-EnKF-t1	96	$t-1, t, t+1$	[32,32,32]	None
VTS-EnKF-t2	96	$t-2, t, t+2$	[32,32,32]	None
VTS-EnKF-t3	96	$t-3, t, t+3$	[32,32,32]	None
VTS-EnKF-t4	96	$t-4, t, t+4$	[32,32,32]	None
VTS-EnKF-t5	96	$t-5, t, t+5$	[32,32,32]	None
VTS-EnKF-t6	96	$t-6, t, t+6$	[32,32,32]	None

4 Results and discussions

The results are discussed in the aspects of assimilation analysis and model forecast. The benefits of using our EnKF with VTS algorithm for the dust storm simulation with position errors are emphasized.

4.1 Impact on assimilation analysis

Figure 4 displays the spatial distribution of ground BR-PM_{10} observations (scatter) and dust field forecasts from the average of the ensembles (panel a.1), the posteriori from EnKF analysis (panel a.2) and EnKF with localization (panel a.3), the average of the enlarged ensembles (panel b.1), the posteriori from VTS-EnKF analysis (panel b.2) and VTS-EnKF analysis with localization (panel b.3) at 11:00, 15th March, 2021 China Standard Time (CST). It should be noted that the average dust concentrations in panel b.1 are calculated from the 160 ensemble simulations used in VTS-EnKF, which slightly differ from the average of 32 ensembles. In DSE1, the RMSE and NMB from the pure ensemble model simulation are as high as 856.36 $\mu g\ m^{-3}$ and -78.31 $\%$. Both EnKF and LEnKF assimilation analyses achieve very limited improvement in estimating the dust state field. As shown in panel a.2 and panel a.3, the RMSE and NMB remain high at 819.04 $\mu g\ m^{-3}$ and -75.65 $\%$ in *EnKF*, and 782.57 $\mu g\ m^{-3}$ and -73.52 $\%$ in *L500*. The main reason for this is the imbalanced uncertainty between the ensemble simulations and the observations, as described in Sect. 3.2. As observed in the light blue box in panel a.1, the simulated dust plume is located farther southeast compared to the PM_{10} measurements. This snapshot exhibits an apparent position error. After EnKF analysis, the simulated dust plume in the light blue box barely changes, as depicted in panel a.2. Numerous ground stations in this area report high PM_{10} concentrations, but the assimilated dust field fails to resolve most of them. The localization method offers limited assistance in this situation, as illustrated in panel a.3. With the unresolved positional error, the EnKF, which focuses more on intensity correction, is much less effective.

When it comes to the VTS-EnKF analysis result, an improved dust field can be noticed. Concerning the Root Mean Square Error (RMSE) and Normalized Mean Bias (NMB), the two priors depicted in panels a.1 and b.1 exhibit highly similar performances. However, slight differences do exist. For instance, the average of the expanded 160-member ensemble used in VTS-EnKF displays a marginally broader spread. The increased ensemble size provides more room for representing background uncertainties. The enhanced capacity for this is best illustrated in Fig. 6 (a), which exhibits the uncertainty quantified by the enlarged ensemble simulations in VTS-EnKF formulations. High uncertainty values are seen in pixels where large model-minus-observation errors are present, such as within the light blue box. This allows the posterior to be adjusted in order to better conform to the observations. In contrast, the relatively low uncertainty over these areas depicted in Fig. 1 (b.2) suggests that the EnKF method is highly confident in the absence of aerosols and does not require any modification. The observations are effectively assimilated in the VTS-EnKF analysis. As displayed in panel b.2, the dust plume within the light blue box is adjusted to better match the observations. In particular, the dust to the east of the marked region is well represented in comparison to the posteriori of *EnKF*. The RMSE and NMB are reduced to 742.33 $\mu g\ m^{-3}$ and -68.21 $\%$. Moreover, the posteriori of *VTS-L500* yields an improved dust field with the RMSE and NMB further reduced to 696.1 $\mu g\ m^{-3}$ and -63.93 $\%$. The implementation of the localization method eliminates spurious correlations and generates a background error covariance

that more accurately describes the model uncertainties. Despite the noticeable improvements achieved in DSE1, the residual errors, as indicated by the RMSE and NMB metrics, remain relatively high. This is mainly due to some observations with extremely high value (exceeding 5000 μg m^{-3}), which is far higher than the surrounding stations and hard for the EnKF to adapt. In particular, the western extent of the dust plume is covered by the insufficient stations, which results in an inadequate representation of the dust load. By incorporating neighboring ensembles, the dust plume is extended wilder, as can't be verified by the observations.

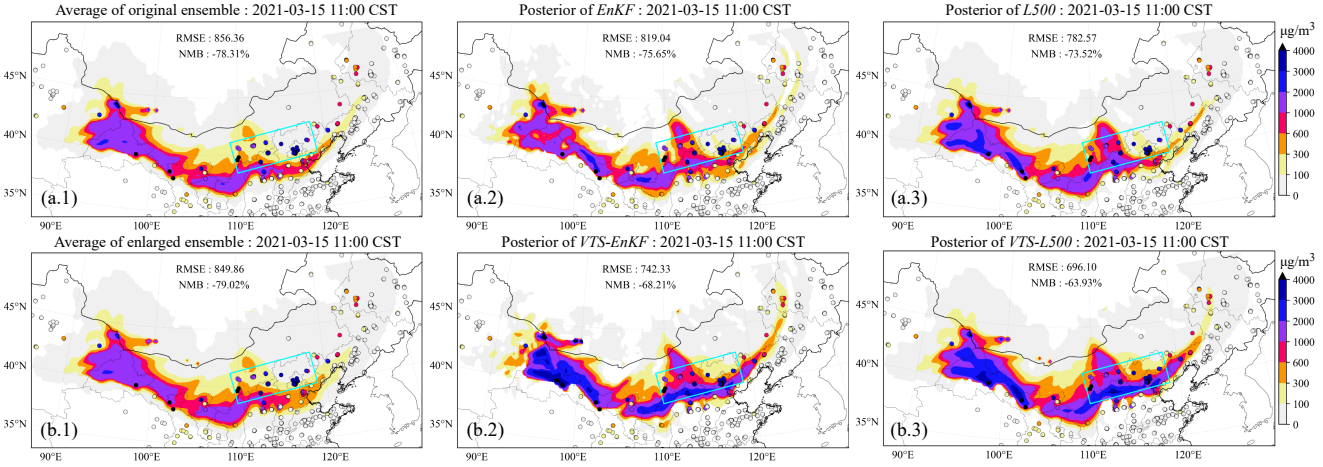

Figure 4. Spatial distribution of ground-based BR-PM_{10} observations (scatter) and simulated dust plume (SDP) on surface from central time ensemble model mean (**a.1**), the posteriori SDP updated by EnKF (**a.2**), the posteriori SDP updated by EnKF with localization (**a.3**), central and neighboring time ensemble model mean (**b.1**), the posteriori SDP updated by VTS-EnKF (**b.2**), the posteriori SDP updated by VTS-EnKF with localization (**b.3**) at 11:00, 15th March 2021 (CST).

Figure 5 presents the spatial distribution of ground-based BR-PM_{10} observations (scatter) and dust concentration forecasts from the average of model ensembles (panel a.1), EnKF (panel a.2), and LEnKF analysis (panel a.3), as well as the average of the enlarged model ensembles (panel b.1), VTS-EnKF (panel b.2), and VTS-EnKF with localization analysis (panel b.3) at 11:00, March 28th, 2021 CST. During this assimilation snapshot in DSE2, the model-simulated dust field is observed to have moved further southeast, as depicted in panel a.1. As illustrated by the light blue box in panel a.1, the model-simulated dust plume missed most of the observations with high PM_{10} concentrations. Consequently, although the EnKF analysis remains effective in this case, dust in light blue box is nearly unchanged. The RMSE and NMB are reduced to 348.13 μg m^{-3} and -45.96 % in the *EnKF* scenario, with further reductions to 301.38 μg m^{-3} and -39.12 % when the localization method is employed in the *L500* case.

For the enlarged ensembles, the RMSE and NMB of the priori for *VTS-EnKF* are 433.08 μg m^{-3} and -8.93 %. With VTS-EnKF assimilation, the RMSE of the posterior further decreases to 246.23 μg m^{-3}, and the NMB is -31.61 % in *VTS-EnKF*. Unlike the *EnKF*, the dust plume in light blue box is noticeably tuned to better fit the observations These error and bias values are significantly lower than those obtained with the *EnKF*, thanks to the better-scaled background covariance displayed in

Fig. 6. Moreover, by incorporating localization, the RMSE and NMB are further reduced to 221.15 μg m^{-3} and -27.23 % in *VTS-L500*. The dust load within the light blue box (panel b.3) is accurately reproduced within its actual range (2000∼3000 μg m^{-3}).

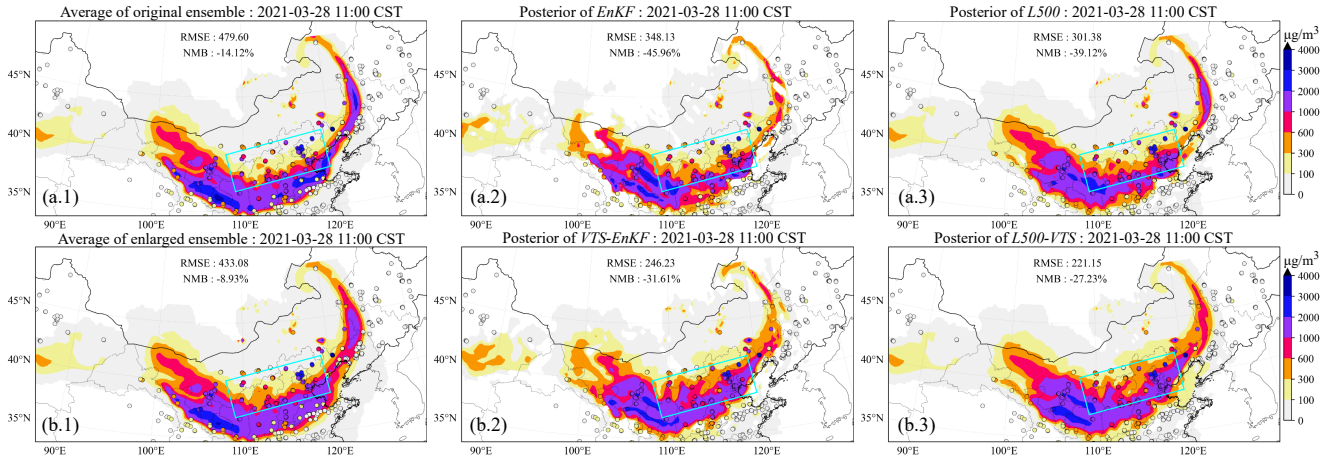

Figure 5. Spatial distribution of ground-based BR-PM_{10} observations (scatter) and simulated dust plume (SDP) on surface from central time ensemble model mean (**a.1**), the posteriori SDP updated by EnKF (**a.2**), the posteriori SDP updated by EnKF with localization (**a.3**), central and neighboring time ensemble model mean (**b.1**), the posteriori SDP updated by VTS-EnKF (**b.2**), the posteriori SDP updated by VTS-EnKF with localization (**b.3**) at 11:00, 28th March 2021 (CST).

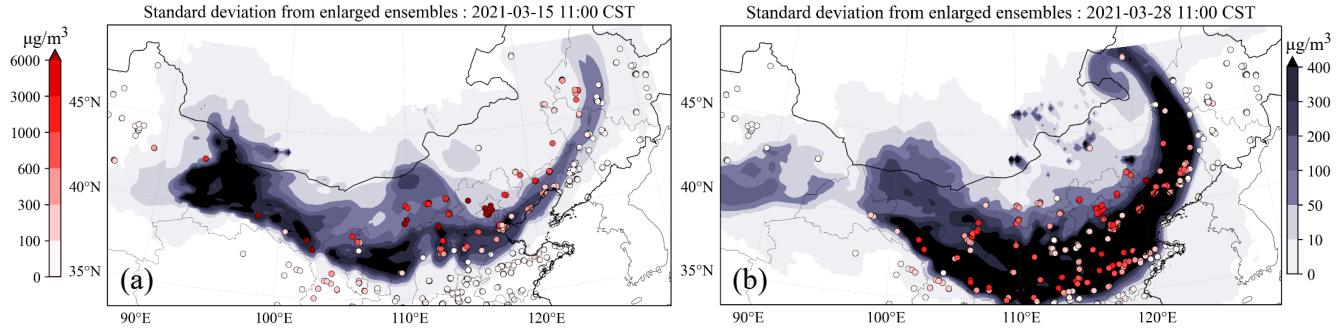

Figure 6. Spatial distribution of standard deviation from model ensembles with scatter of model-minus-observation differences (absolute value) at 11:00 in DSE1(**a**) and 08:00 in DSE2(**b**). The initial assimilation analysis is performed at these time. Colorbar left is for model-minus-observation differences and right is for standard deviation.

4.2 Impact on forecast skills

In addition to the snapshots of the assimilation analysis, an comprehensive evaluation of forecast skills is also necessary to see the performance of VTS-EnKF algorithm. A general evaluation on the forecasting skills is carried out in this section.

Figure 7 presents the time series of RMSE and NMB for the 24-hour dust forecast after three assimilation analyses in DSE1 (starting from 11:00, 14:00, and 17:00). In these cases, the *Control run* generates a dust field with a high RMSE (ranging from over 800 $\mu g\ m^{-3}$ to around 600 $\mu g\ m^{-3}$) and a large NMB (consistently around -85 $\%$). The EnKF analysis, however, does not improve this dust forecast after the initial assimilation. In fact, the RMSE and NMB of the dust forecast from the *EnKF* scenario are nearly identical to the *Control run*, as evidenced by the comparison between the black dashed line and the blue line in panel a. This result can be primarily attributed to the position error discussed in Sect. 2.4. The EnKF algorithm offers minimal assistance in correcting the model simulation when position errors are present. These errors are not occasional but cumulative, as demonstrated in the subsequent two assimilation timestamps at 14:00 and 17:00, during which the assimilation analysis shows limited improvement over the situation. Moreover, it has been observed that the localization method is unable to enhance the forecast in the presence of position errors. Similar for NMB, as depicted in panel b, the improvements are also insignificant. The NMB for the *Control*, *EnKF*, and *L500* scenarios remains consistently around -85 $\%$ throughout the entire forecast time range.

By applying the VTS-EnKF analysis, a reduction of RMSE is observed in panel a. There is an approximate decrease of 100 $\mu g\ m^{-3}$ in *VTS-EnKF* compared to *EnKF*, which indicates that the VTS-EnKF analysis effectively corrects the position error. At the subsequent assimilation timestamps, this situation improves, with an even greater decrease in RMSE. The RMSE of *VTS-L500* is slightly lower than that of *VTS-EnKF*. As for NMB, quite promising results are achieved. In *VTS-EnKF*, the NMB decreases stepwise at three time points, from around -75 $\%$ at 11:00 to around -70 $\%$ at 14:00, and finally to around -65 $\%$. The VTS-EnKF algorithm gradually takes effect over the three assimilation analyses. In *VTS-L500*, the localization method demonstrates its efficacy, especially after the third assimilation timestamp at 17:00. The NMB is reduced to around -60 $\%$, which is significantly lower than that of the *L500*.

Figure 8 displays the time series of RMSE and NMB on a 24-hour dust forecast after three assimilation analyses in DSE2. Unlike DSE1, *EnKF* in DSE2 does improve the dust forecast in terms of RMSE and NMB. The RMSE drops from around 500 $\mu g\ m^{-3}$ to less than 400 $\mu g\ m^{-3}$ at the initial assimilation timestamp (11:00). NMB here is higher than *Control* due to the complementary effect of NMB. The overestimation is corrected while the underestimation caused by position error is not corrected. No further reduction is observed at subsequent time points. As can be seen in panels a.2 and a.3, the RMSE of *EnKF* remains almost constant compared to panel a.1. This indicates that the position error is not corrected, and it constitutes part of the RMSE that is difficult to eliminate. The trend of NMB also reflects this situation. *L500* is unable to correct the position error, although it does help reduce the error to some extent.

In the scenario of the VTS-EnKF analysis, an improvement in the dust forecast of DSE2 is obtained. A general reduction of RMSE (around 50 $\mu g\ m^{-3}$) in *VTS-EnKF* compared to *EnKF* can be seen in panel a.1. Furthermore, in the subsequent forecasts, a steady decrease in RMSE is noted. The RMSE fluctuates around 250 $\mu g\ m^{-3}$ after 14:00 and 200 $\mu g\ m^{-3}$ after

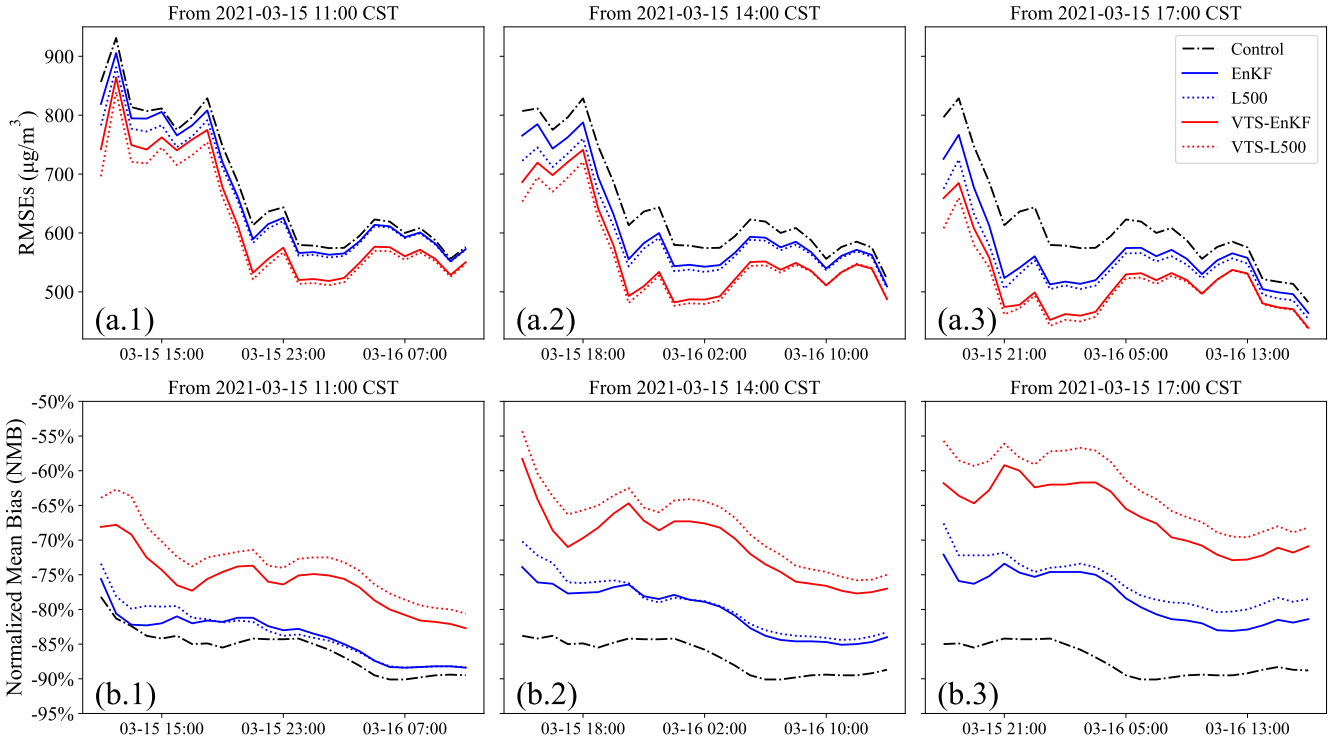

Figure 7. Time series of 24-hour Root Mean Square Error (RMSE) on the dust forecast starting from 11:00 (**a.1**), 14:00 (**a.2**), 17:00 (**a.3**) and normalized mean bias (NMB) starting from 11:00 (**b.1**), 14:00 (**b.2**), 17:00 (**b.3**) on 15th March 2021.

17:00. *VTS-L500* exhibits a similar pattern to *VTS-EnKF* for most of the forecast. Considering the NMB, as shown in panel b, the NMB of *VTS-L500* demonstrates trivial superiority over *VTS-EnKF*. In DSE2, the *EnKF* and *L500* have already achieved well-reproduced dust fields, while the *VTS-EnKF* and *VTS-L500* can further improve these fields by correcting the position error.

4.3 Assessment of smaller ensembles

To further assess the performance of VTS-EnKF, VTS-EnKF experiments with same ensembles as the EnKF are designed. They are referred to as *VTS-EnKF-small* and *VTS-L500-small*, respectively. The total 32 ensembles are composed of 8 central ensembles and 4×6 ensembles from neighboring ±1 and ±2 hours. Figure 9 displays the time series of RMSE and NMB on a 24-hour dust forecast after three assimilation analyses in DSE1. In terms of RMSE, *VTS-EnKF-small* only shows slightly better performance than the EnKF. This mostly caused by the sampling error arises from limited ensembles resampled from the central ensembles (only 8 ensembles). However, by applying the localization, the RMSE is noticeably reduced by 100 μg m^{-3}. The performance is comparable to the *VTS-L500* (red dash line) with totally 160 ensembles. By mitigating the sampling error, the VTS-EnKF's capability of handling the position error can be revealed, which can be noticed by comparison with

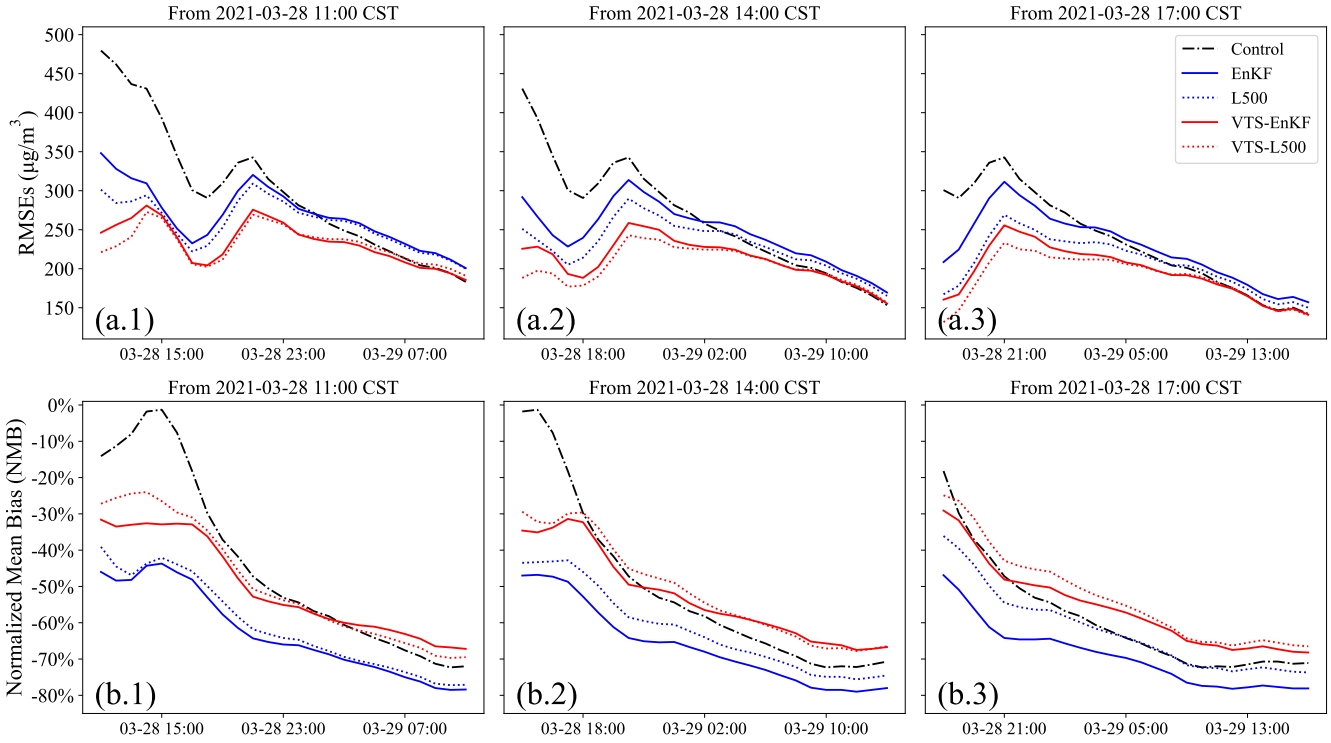

Figure 8. Time series of 24-hour Root Mean Square Error (RMSE) on the dust forecast starting from 08:00 (**a.1**), 11:00 (**a.2**), 14:00 (**a.3**) and normalized mean bias (NMB) starting from 08:00 (**b.1**), 11:00 (**b.2**), 15:00 (**b.3**) on 28th March 2021.

L500 and *VTS-L500-small*. This improvement can be better seen in NMB. NMB of *VTS-L500-small* is much lower than the *EnKF* and *L500*. Its performance is also comparable to the *VTS-L500* with 160 ensembles.

Same experiments on DSE2 are also carried out. Results can be found in Fig. S2 in supporting information. Similar to DSE1, the *VTS-EnKF-small* achieves slightly better RMSE and NMB than *EnKF* and *L500*. While in *VTS-L500-small*, noticeable improvements can been found especially for the forecast after the second and last assimilation. Reduction of 100 μg m^{-3} in RMSE and 20% in NMB are obtained.

4.4 Sensitivity of time interval

Previous researches have found that an improper neighboring time interval τ can lead to undesirable results, such as less-effective ensemble members (interval too small) (τ too small) or ensemble member clustering and unrepresentative ensemble covariances (τ too large) (Xu et al., 2008; Gasperoni et al., 2022, 2023). To explore the sensitivity of the choice of neighboring time interval, series of VTS-EnKF experiments with different neighboring time interval were carries out. Time intervals ranging from 1 to 6 hour were tested. As shown in Fig. 10, snapshots from 6 experiments on DSE1 clearly depicts the trend. In general, all the VTS-EnKF experiments show better performance than EnKF. While in terms of specific time interval, different patterns

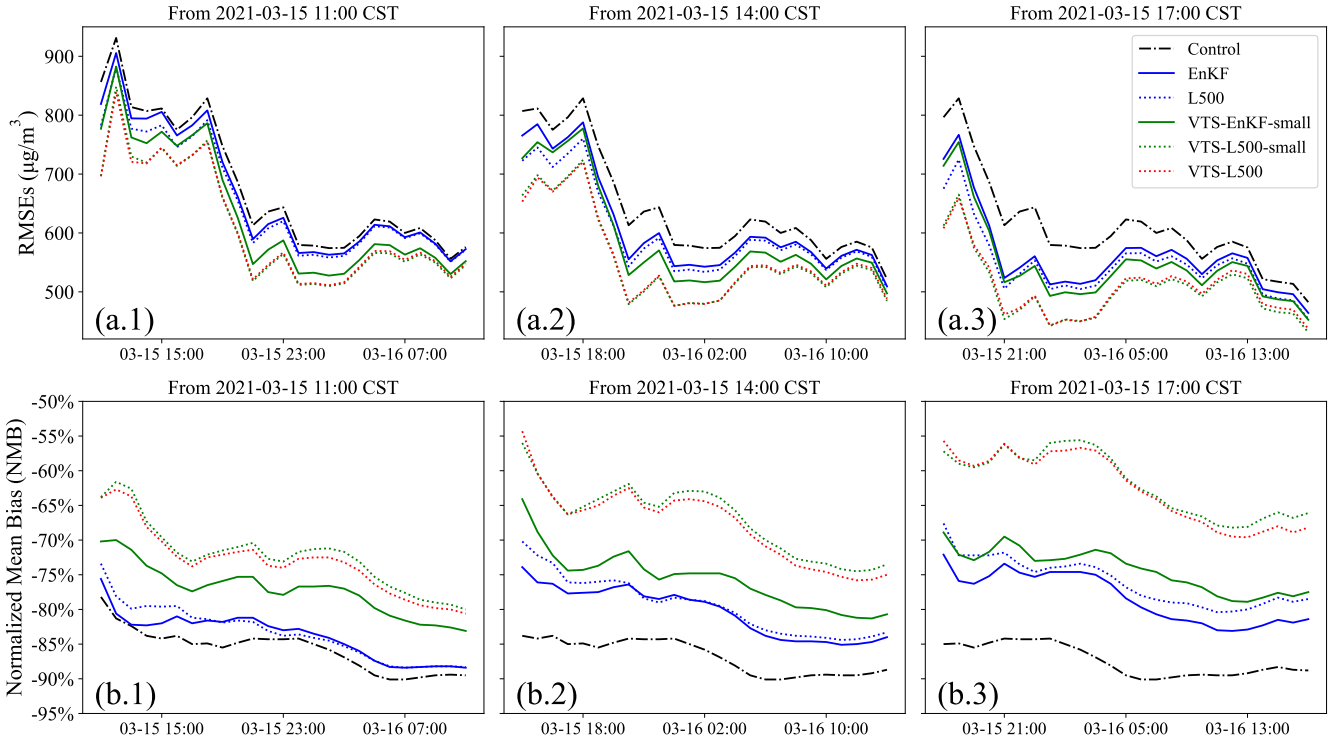

Figure 9. Time series of 24-hour Root Mean Square Error (RMSE) on the dust forecast starting from 11:00 (**a.1**), 14:00 (**a.2**), 17:00 (**a.3**) and normalized mean bias (NMB) starting from 11:00 (**b.1**), 14:00 (**b.2**), 17:00 (**b.3**) on 15th March 2021.

can be noticed. For short intervals including 1 and 2 hour, there is not sufficient ensemble spread to account for the position error. Thus there are still position error remaining and RMSE is still high. For long intervals including 5 and 6 hour, dust plume is clustered away from central dust plume. Three dust branches are noticed in *VTS-EnKF-t5* and an overly backwards dust plume is noticed in *VTS-EnKF-t6*. In this case, 3-hour interval is the best choice with the lowest RMSE (696.11 μg m^{-3}) and NMB (-63.5 %).

Same experiments on DSE2 are also performed and snapshots are shown in Fig. S3. Similar patterns are found on DSE2. Lowest RMSE and NMB are achieved in *VTS-EnKF-t4*. Too short interval leads to inability in position error correction and too long interval leads to excessive dust plume. Considering both cases, 3-hour interval is the preferred choice which holds the capability to handle position and not creates excessive clustered dust plume.

5 Conclusions

The Chemistry Transport Model (CTM) is a powerful tool for air pollutant forecasting. However, as a simplified version of the real atmospheric world, it suffers from various deficiencies, particularly in two major uncertainties: emissions and

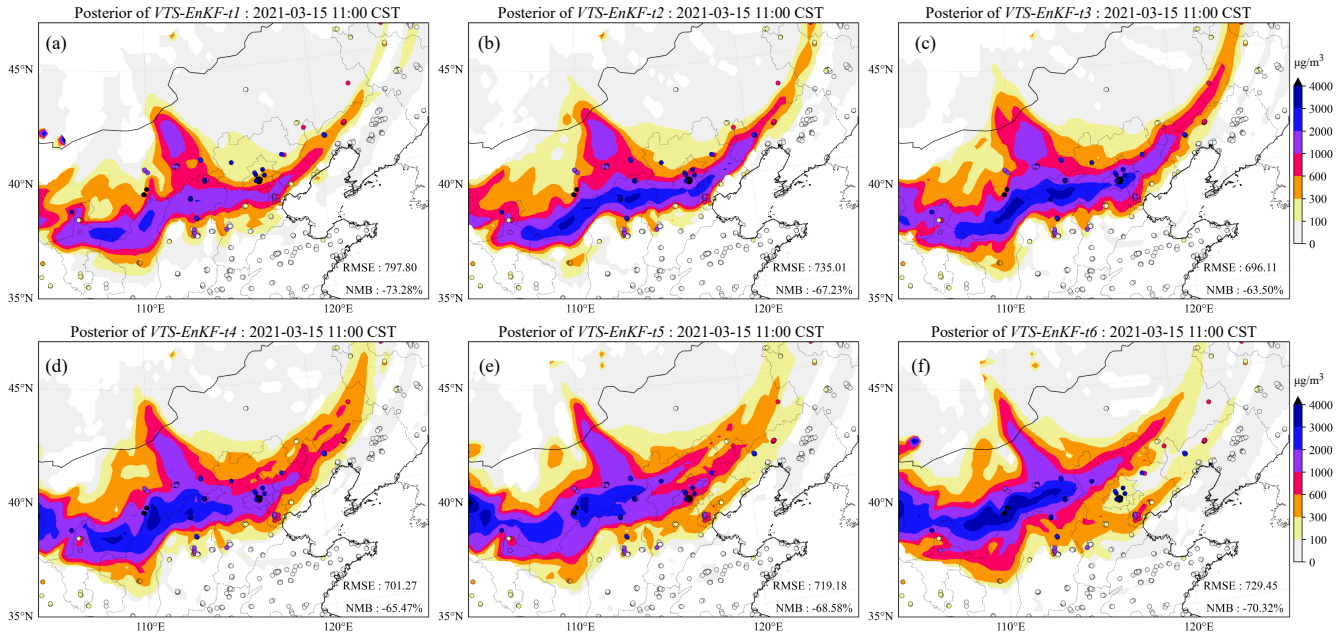

Figure 10. Spatial distribution of ground-based BR-PM_{10} observations (scatter) and simulated dust plume (SDP) on surface from the posteriori SDP updated by VTS-EnKF-t1 (**a**), the posteriori SDP updated by VTS-EnKF-t2 (**b**), the posteriori SDP updated by VTS-EnKF-t3 (**c**), the posteriori SDP updated by VTS-EnKF-t4 (**d**), the posteriori SDP updated by VTS-EnKF-t5 (**e**), the posteriori SDP updated by VTS-EnKF-t6 (**f**) at 11:00, 15th March 2021 (CST).

meteorology. Uncertainty from meteorological fields can cause model forecast errors, especially in long-distance transport. In dust storm forecasting applications, a position error is noted that significantly degrades the overall performance of the forecast and prevents the EnKF assimilation algorithm from effectively incorporating observational data.

The background error covariance of EnKF is generally designed to represent the intensity and position uncertainty. However, when the position error is sufficiently large, the background error covariance can't adequately represent the position error, which is highly non-Gaussian. In the case of the long-distance dust storm tracking, the EnKF is incapable of thoroughly resolving the observations. Observations over low model uncertainty pixels are 'ignored' by the EnKF algorithm. To address this issue, a valid time shifting method is coupled with EnKF . This VTS-EnKF methodology introduces uncertainty of the dust plume position into the background error covariance by incorporating extra ensemble simulations at neighboring time instances. This enlarged ensemble not only reflects the uncertainty of dust intensity but also reveals the potential positions of the plume, allowing for more accurate and effective assimilation and improving dust storm forecasting.

The VTS-EnKF algorithm was tested on two super dust storm events (DSE1 and DSE2) that occurred in Spring 2021. Several experiments were designed to examine the performance of the VTS-EnKF algorithm in these cases, with a focus on differences between EnKF and VTS-EnKF. In terms of assimilation analysis, the VTS-EnKF analysis corrected the position error in DSE1 to a large extent. Comparison between the standard deviations from posterior of EnKF and VTS-EnKF explained

for it. The standard deviations from VTS-EnKF analysis indicated wilder potential dust spread and were more consistent with the model-minus-observation. Observations that were 'ignored' by EnKF were comprehensively resolved in VTS-EnKF, resulting in decreased RMSE and NMB. For DSE2, the position error was not as significant as in DSE1; however, imbalanced uncertainties were also observed. Nevertheless, VTS-EnKF still produced an improved dust field with lower RMSE and NMB compared to EnKF. In both cases, the localization method helped reduce RMSE and NMB. Regarding the forecast performance, promising results were obtained. In DSE1, the RMSE and NMB revealed that EnKF provides limited improvements compared to model run. In contrast, VTS-EnKF provided a dust field forecast with reduced errors, especially in terms of NMB. Additionally, the localization method contributed to further reducing the error. Overall, the VTS-EnKF algorithm demonstrated improved performance in assimilation analysis and forecasting for the tested dust storm events compared to the traditional EnKF approach.

Assessment of equal ensembles between EnKF and VTS-EnKF is carried out. VTS-EnKF with smaller ensembles shows slightly improved metrics than EnKF. While by applying localization, more reduction in RMSE and NMB can be noticed and its performance is comparable to the VTS-EnKF with larger ensembles. This is due to the corrected sampling error within limited ensembles. Comparison between them confirms VTS-EnKF's ability in handling position error. Sensitivity of neighboring time interval choice is also examined. Too short interval leads to inability in position error correction and too long interval leads to excessive dust plume. Considering both cases, 3-hour interval is the preferred choice.

Code and data availability. The EnKF with VTS code is archived on Zenodo at https://doi.org/10.5281/zenodo.7611976 (Pang, last access: Nov. 2023). The PM_{10} data used in this study is also archived on Zenodo at https://doi.org/10.5281/zenodo.6459866 (Jin, 2022). The real-time PM_{10} data established by the Ministry of Ecology and Environment is available to the public at https://quotsoft.net/air (Wang, last access: Nov. 2023). The source code and user guide of the LOTOS-EUROS model could be obtained from https://lotos-euros.tno.nl (TNO, last access: August 2023).

Author contributions. JJ conceived the study and designed VTS-EnKF algorithm. MP wrote the code of the assimilation and carried out the experiments and evaluation. AS, HJ, WH, BB, JX, LF, JL, HXL and HL provided useful comments on the paper. MP and JJ prepared the manuscript with contributions from HJ and all others co-authors.

Acknowledgements. This work is supported by the National Natural Science Foundation of China [grant No. 42105109 and 42205031] and Natural Science Foundation of Jiangsu Province (No. BK20210664).

Competing interests

The authors declare that they have no conflict of interest.

References

Amezcua, J. and Van Leeuwen, P. J.: Gaussian Anamorphosis in the Analysis Step of the EnKF: A Joint State-Variable/Observation Approach, TELLUS A, 66, 23 493, https://doi.org/10.3402/tellusa.v66.23493, 2014.

An, L., Che, H., Xue, M., Zhang, T., Wang, H., Wang, Y., Zhou, C., Zhao, H., Gui, K., Zheng, Y., Sun, T., Liang, Y., Sun, E., Zhang, H., and Zhang, X.: Temporal and Spatial Variations in Sand and Dust Storm Events in East Asia from 2007 to 2016: Relationships with Surface Conditions and Climate Change, Sci. Total Environ., 633, 452–462, https://doi.org/10.1016/j.scitotenv.2018.03.068, 2018.

Bannister, R. N.: A Review of Operational Methods of Variational and Ensemble-Variational Data Assimilation, Q. J. R. Meteorolog. Soc., 143, 607–633, https://doi.org/10.1002/qj.2982, 2017.

Bergamaschi, P., Krol, M., Meirink, J. F., Dentener, F., Segers, A., van Aardenne, J., Monni, S., Vermeulen, A. T., Schmidt, M., Ramonet, M., Yver, C., Meinhardt, F., Nisbet, E. G., Fisher, R. E., O'Doherty, S., and Dlugokencky, E. J.: Inverse Modeling of European CH_4 Emissions 2001–2006, J. Geophys. Res., 115, D22 309, https://doi.org/10.1029/2010JD014180, 2010.

Brasseur, G. P., Xie, Y., Petersen, A. K., Bouarar, I., Flemming, J., Gauss, M., Jiang, F., Kouznetsov, R., Kranenburg, R., Mijling, B., Peuch, V.-H., Pommier, M., Segers, A., Sofiev, M., Timmermans, R., van der A, R., Walters, S., Xu, J., and Zhou, G.: Ensemble Forecasts of Air Quality in Eastern China – Part 1: Model Description and Implementation of the MarcoPolo–Panda Prediction System, Version 1, Geosci. Model Dev., 12, 33–67, https://doi.org/10.5194/gmd-12-33-2019, 2019.

Brewster, K. A.: Phase-Correcting Data Assimilation and Application to Storm-Scale Numerical Weather Prediction. Part I: Method Description and Simulation Testing, Mon. Weather Rev., 131, 480–492, https://doi.org/10.1175/1520-0493(2003)131<0480:PCDAAA>2.0.CO;2, 2003.

Brunner, D., Henne, S., Keller, C. A., Reimann, S., Vollmer, M. K., O'Doherty, S., and Maione, M.: An Extended Kalman-filter for Regional Scale Inverse Emission Estimation, Atmos. Chem. Phys., 12, 3455–3478, https://doi.org/10.5194/acp-12-3455-2012, 2012.

Burgers, G., Jan van Leeuwen, P., and Evensen, G.: Analysis Scheme in the Ensemble Kalman Filter, Mon. Weather Rev., 126, 1719–1724, https://doi.org/10.1175/1520-0493(1998)126<1719:ASITEK>2.0.CO;2, 1998.

Chen, L. and Walsh, M.: Vast Sandstorms Expose Mongolia's Long-Ignored Ecological Crisis, 2021.

Corazza, M., Bergamaschi, P., Vermeulen, A. T., Aalto, T., Haszpra, L., Meinhardt, F., O'Doherty, S., Thompson, R., Moncrieff, J., Popa, E., Steinbacher, M., Jordan, A., Dlugokencky, E., Brühl, C., Krol, M., and Dentener, F.: Inverse Modelling of European N_2O Emissions: Assimilating Observations from Different Networks, Atmos. Chem. Phys., 11, 2381–2398, https://doi.org/10.5194/acp-11-2381-2011, 2011.

Curier, R., Timmermans, R., Calabretta-Jongen, S., Eskes, H., Segers, A., Swart, D., and Schaap, M.: Improving Ozone Forecasts over Europe by Synergistic Use of the LOTOS-EUROS Chemical Transport Model and in-Situ Measurements, Atmos. Environ., 60, 217–226, https://doi.org/10.1016/j.atmosenv.2012.06.017, 2012.

Dance, S. L.: Issues in High Resolution Limited Area Data Assimilation for Quantitative Precipitation Forecasting, Physica D, 196, 1–27, https://doi.org/10.1016/j.physd.2004.05.001, 2004.

Di Tomaso, E., Schutgens, N. A. J., Jorba, O., and Pérez García-Pando, C.: Assimilation of MODIS Dark Target and Deep Blue Observations in the Dust Aerosol Component of NMMB-MONARCH Version 1.0, Geosci. Model Dev., 10, 1107–1129, https://doi.org/10.5194/gmd-10-1107-2017, 2017.

Di Tomaso, E., Escribano, J., Basart, S., Ginoux, P., Macchia, F., Barnaba, F., Benincasa, F., Bretonnière, P.-A., Buñuel, A., Castrillo, M., Cuevas, E., Formenti, P., Gonçalves, M., Jorba, O., Klose, M., Mona, L., Montané Pinto, G., Mytilinaios, M., Obiso, V., Olid, M.,

Schutgens, N., Votsis, A., Werner, E., and Pérez García-Pando, C.: The MONARCH High-Resolution Reanalysis of Desert Dust Aerosol over Northern Africa, the Middle East and Europe (2007–2016), Earth Syst. Sci. Data, 14, 2785–2816, https://doi.org/10.5194/essd-14-2785-2022, 2022.

Duncan Fairlie, T., Jacob, D. J., and Park, R. J.: The Impact of Transpacific Transport of Mineral Dust in the United States, Atmos. Environ., 41, 1251–1266, https://doi.org/10.1016/j.atmosenv.2006.09.048, 2007.

Escribano, J., Boucher, O., Chevallier, F., and Huneeus, N.: Impact of the Choice of the Satellite Aerosol Optical Depth Product in a Sub-Regional Dust Emission Inversion, Atmos. Chem. Phys., 17, 7111–7126, https://doi.org/10.5194/acp-17-7111-2017, 2017.

Evensen, G.: Sequential Data Assimilation with a Nonlinear Quasi-Geostrophic Model Using Monte Carlo Methods to Forecast Error Statistics, J. Geophys. Res., 99, 10 143, https://doi.org/10.1029/94JC00572, 1994.

Filonchyk, M. and Peterson, M.: Development, Progression, and Impact on Urban Air Quality of the Dust Storm in Asia in March 15–18, 2021, Urban Clim., 41, 101 080, https://doi.org/10.1016/j.uclim.2021.101080, 2022.

Foroutan, H. and Pleim, J. E.: Improving the Simulation of Convective Dust Storms in Regional-to-Global Models, J. Adv. Model. Earth Syst., 9, 2046–2060, https://doi.org/10.1002/2017MS000953, 2017.

Foroutan, H., Young, J., Napelenok, S., Ran, L., Appel, K. W., Gilliam, R. C., and Pleim, J. E.: Development and Evaluation of a Physics-Based Windblown Dust Emission Scheme Implemented in the CMAQ Modeling System, J. Adv. Model. Earth Syst., 9, 585–608, https://doi.org/10.1002/2016MS000823, 2017.

Gaspari, G. and Cohn, S. E.: Construction of Correlation Functions in Two and Three Dimensions, Q. J. R. Meteorolog. Soc., 125, 723–757, https://doi.org/10.1002/qj.49712555417, 1999.

Gasperoni, N. A., Wang, X., and Wang, Y.: Using a Cost-Effective Approach to Increase Background Ensemble Member Size within the GSI-Based EnVar System for Improved Radar Analyses and Forecasts of Convective Systems, Mon. Weather Rev., 150, 667–689, https://doi.org/10.1175/MWR-D-21-0148.1, 2022.

Gasperoni, N. A., Wang, X., and Wang, Y.: Valid Time Shifting for an Experimental RRFS Convection-Allowing EnVar Data Assimilation and Forecast System: Description and Systematic Evaluation in Real Time, Mon. Weather Rev., 151, 1229–1245, https://doi.org/10.1175/MWR-D-22-0089.1, 2023.

Ginoux, P., Chin, M., Tegen, I., Prospero, J. M., Holben, B., Dubovik, O., and Lin, S.-J.: Sources and Distributions of Dust Aerosols Simulated with the GOCART Model, J. Geophys. Res., 106, 20 255–20 273, https://doi.org/10.1029/2000JD000053, 2001.

Ginoux, P., Prospero, J. M., Gill, T. E., Hsu, N. C., and Zhao, M.: Global-Scale Attribution of Anthropogenic and Natural Dust Sources and Their Emission Rates Based on MODIS Deep Blue Aerosol Products, Rev. Geophys., 50, https://doi.org/10.1029/2012RG000388, 2012.

Gong, S. L. and Zhang, X. Y.: CUACE/Dust – an Integrated System of Observation and Modeling Systems for Operational Dust Forecasting in Asia, Atmos. Chem. Phys., 8, 2333–2340, https://doi.org/10.5194/acp-8-2333-2008, 2008.

Goudie, A. S.: Desert Dust and Human Health Disorders, Environ. Int., 63, 101–113, https://doi.org/10.1016/j.envint.2013.10.011, 2014.

Gross, J. E., Carlos, W. G., Dela Cruz, C. S., Harber, P., and Jamil, S.: Sand and Dust Storms: Acute Exposure and Threats to Respiratory Health, AM J RESP CRIT CARE, 198, P13–P14, https://doi.org/10.1164/rccm.1987P13, 2018.

Gui, K., Yao, W., Che, H., An, L., Zheng, Y., Li, L., Zhao, H., Zhang, L., Zhong, J., Wang, Y., and Zhang, X.: Record-Breaking Dust Loading during Two Mega Dust Storm Events over Northern China in March 2021: Aerosol Optical and Radiative Properties and Meteorological Drivers, Atmos. Chem. Phys., 22, 7905–7932, https://doi.org/10.5194/acp-22-7905-2022, 2022.

Hamill, T. M.: Ensemble-Based Atmospheric Data Assimilation, in: Predictability of Weather and Climate, edited by Palmer, T. and Hagedorn, R., pp. 124–156, Cambridge University Press, 1 edn., https://doi.org/10.1017/CBO9780511617652.007, 2006.

Houtekamer, P. L. and Zhang, F.: Review of the Ensemble Kalman Filter for Atmospheric Data Assimilation, Mon. Weather Rev., 144, 4489–4532, https://doi.org/10.1175/MWR-D-15-0440.1, 2016.

Houtekamer, P. L., Mitchell, H. L., Pellerin, G., Buehner, M., Charron, M., Spacek, L., and Hansen, B.: Atmospheric Data Assimilation with an Ensemble Kalman Filter: Results with Real Observations, Mon. Weather Rev., 133, 604–620, https://doi.org/10.1175/MWR-2864.1, 2005.

Houtekamer, P. L., Deng, X., Mitchell, H. L., Baek, S.-J., and Gagnon, N.: Higher Resolution in an Operational Ensemble Kalman Filter, Mon. Weather Rev., 142, 1143–1162, https://doi.org/10.1175/MWR-D-13-00138.1, 2014.

Hu, Z., Huang, J., Zhao, C., Bi, J., Jin, Q., Qian, Y., Leung, L. R., Feng, T., Chen, S., and Ma, J.: Modeling the Contributions of Northern Hemisphere Dust Sources to Dust Outflow from East Asia, Atmos. Environ., 202, 234–243, https://doi.org/10.1016/j.atmosenv.2019.01.022, 2019.

Huang, B. and Wang, X.: On the Use of Cost-Effective Valid-Time-Shifting (VTS) Method to Increase Ensemble Size in the GFS Hybrid 4DEnVar System, Mon. Weather Rev., 146, 2973–2998, https://doi.org/10.1175/MWR-D-18-0009.1, 2018.

Jin, G.: The Most Severe Sandstorm in a Decade, 2021.

Jin, J.: Ground-Based Air Quality Measurements during the 2021 Spring Super Dust Storms, https://doi.org/10.5281/zenodo.6459866, 2022.

Jin, J., Lin, H. X., Heemink, A., and Segers, A.: Spatially Varying Parameter Estimation for Dust Emissions Using Reduced-Tangent-Linearization 4DVar, Atmos. Environ., 187, 358–373, https://doi.org/10.1016/j.atmosenv.2018.05.060, 2018.

Jin, J., Lin, H. X., Segers, A., Xie, Y., and Heemink, A.: Machine Learning for Observation Bias Correction with Application to Dust Storm Data Assimilation, Atmos. Chem. Phys., 19, 10 009–10 026, https://doi.org/10.5194/acp-19-10009-2019, 2019a.

Jin, J., Segers, A., Heemink, A., Yoshida, M., Han, W., and Lin, H.-X.: Dust Emission Inversion Using Himawari-8 AODs Over East Asia: An Extreme Dust Event in May 2017, J. Adv. Model. Earth Syst., 11, 446–467, https://doi.org/10.1029/2018MS001491, 2019b.

Jin, J., Segers, A., Liao, H., Heemink, A., Kranenburg, R., and Lin, H. X.: Source Backtracking for Dust Storm Emission Inversion Using an Adjoint Method: Case Study of Northeast China, Atmos. Chem. Phys., 20, 15 207–15 225, https://doi.org/10.5194/acp-20-15207-2020, 2020.

Jin, J., Segers, A., Lin, H. X., Henzing, B., Wang, X., Heemink, A., and Liao, H.: Position Correction in Dust Storm Forecasting Using LOTOS-EUROS v2.1: Grid-Distorted Data Assimilation v1.0, Geosci. Model Dev., 14, 5607–5622, https://doi.org/10.5194/gmd-14-5607-2021, 2021.

Jin, J., Pang, M., Segers, A., Han, W., Fang, L., Li, B., Feng, H., Lin, H. X., and Liao, H.: Inverse Modeling of the 2021 Spring Super Dust Storms in East Asia, Atmos. Chem. Phys., 22, 6393–6410, https://doi.org/10.5194/acp-22-6393-2022, 2022.

Kalman, R. E.: A New Approach to Linear Filtering and Prediction Problems, J. Basic Eng., 82, 35–45, https://doi.org/10.1115/1.3662552, 1960.

Katzfuss, M., Stroud, J. R., and Wikle, C. K.: Understanding the Ensemble Kalman Filter, The American Statistician, 70, 350–357, https://doi.org/10.1080/00031305.2016.1141709, 2016.

Kok, J. F., Mahowald, N. M., Fratini, G., Gillies, J. A., Ishizuka, M., Leys, J. F., Mikami, M., Park, M.-S., Park, S.-U., Van Pelt, R. S., and Zobeck, T. M.: An Improved Dust Emission Model – Part 1: Model Description and Comparison against Measurements, Atmos. Chem. Phys., 14, 13 023–13 041, https://doi.org/10.5194/acp-14-13023-2014, 2014.

Kranenburg, R., Segers, A. J., Hendriks, C., and Schaap, M.: Source Apportionment Using LOTOS-EUROS: Module Description and Evaluation, Geosci. Model Dev., 6, 721–733, https://doi.org/10.5194/gmd-6-721-2013, 2013.

Law, K. J. H. and Stuart, A. M.: Evaluating Data Assimilation Algorithms, Mon. Weather Rev., 140, 3757–3782, https://doi.org/10.1175/MWR-D-11-00257.1, 2012.

Leeuwen, P. J., Künsch, H. R., Nerger, L., Potthast, R., and Reich, S.: Particle Filters for High-dimensional Geoscience Applications: A Review, Q. J. R. Meteorolog. Soc., 145, 2335–2365, https://doi.org/10.1002/qj.3551, 2019.

Lei, J., Bickel, P., and Snyder, C.: Comparison of Ensemble Kalman Filters under Non-Gaussianity, Mon. Weather Rev., 138, 1293–1306, https://doi.org/10.1175/2009MWR3133.1, 2010.

Liu, Y., Xing, J., Wang, S., Fu, X., and Zheng, H.: Source-Specific Speciation Profiles of $PM_{2.5}$ for Heavy Metals and Their Anthropogenic Emissions in China, Environ. Pollut., 239, 544–553, https://doi.org/10.1016/j.envpol.2018.04.047, 2018.

Lopez-Restrepo, S., Yarce, A., Pinel, N., Quintero, O., Segers, A., and Heemink, A.: Forecasting PM_{10} and $PM_{2.5}$ in the Aburrá Valley (Medellín, Colombia) via EnKF Based Data Assimilation, Atmos. Environ., 232, 117 507, https://doi.org/10.1016/j.atmosenv.2020.117507, 2020.

Lu, H., Xu, Q., Yao, M., and Gao, S.: Time-Expanded Sampling for Ensemble-Based Filters: Assimilation Experiments with Real Radar Observations, Adv. Atmos. Sci., 28, 743–757, https://doi.org/10.1007/s00376-010-0021-4, 2011.

Mallet, V. and Sportisse, B.: Uncertainty in a Chemistry-Transport Model Due to Physical Parameterizations and Numerical Approximations: An Ensemble Approach Applied to Ozone Modeling, J. Geophys. Res., 111, https://doi.org/10.1029/2005JD006149, 2006.

Manders, A. M. M., Builtjes, P. J. H., Curier, L., Denier van der Gon, H. A. C., Hendriks, C., Jonkers, S., Kranenburg, R., Kuenen, J. J. P., Segers, A. J., Timmermans, R. M. A., Visschedijk, A. J. H., Wichink Kruit, R. J., van Pul, W. A. J., Sauter, F. J., van der Swaluw, E., Swart, D. P. J., Douros, J., Eskes, H., van Meijgaard, E., van Ulft, B., van Velthoven, P., Banzhaf, S., Mues, A. C., Stern, R., Fu, G., Lu, S., Heemink, A., van Velzen, N., and Schaap, M.: Curriculum Vitae of the LOTOS–EUROS (v2.0) Chemistry Transport Model, Geosci. Model Dev., 10, 4145–4173, https://doi.org/10.5194/gmd-10-4145-2017, 2017.

Marticorena, B. and Bergametti, G.: Modeling the Atmospheric Dust Cycle: 1. Design of a Soil-Derived Dust Emission Scheme, J. Geophys. Res., 100, 16 415, https://doi.org/10.1029/95JD00690, 1995.

Mona, L., Papagiannopoulos, N., Basart, S., Baldasano, J., Binietoglou, I., Cornacchia, C., and Pappalardo, G.: EARLINET Dust Observations vs. BSC-DREAM8b Modeled Profiles: 12-Year-Long Systematic Comparison at Potenza, Italy, Atmos. Chem. Phys., 14, 8781–8793, https://doi.org/10.5194/acp-14-8781-2014, 2014.

Muhammad Akhlaq, Sheltami, T. R., and Mouftah, H. T.: A Review of Techniques and Technologies for Sand and Dust Storm Detection, Rev .Environ. Sci. Bio., 11, 305–322, https://doi.org/10.1007/s11157-012-9282-y, 2012.

Nehrkorn, T., Woods, B. K., Hoffman, R. N., and Auligné, T.: Correcting for Position Errors in Variational Data Assimilation, Mon. Weather Rev., 143, 1368–1381, https://doi.org/10.1175/MWR-D-14-00127.1, 2015.

Pang, M.: Source Code of PyFilter, Zenodo, https://doi.org/10.5281/zenodo.7611976, last access: Nov. 2023.

Pang, M., Jin, J., Segers, A., Jiang, H., Fang, L., Lin, H. X., and Liao, H.: Dust Storm Forecasting through Coupling LOTOS-EUROS with Localized Ensemble Kalman Filter, Atmos. Environ., 306, 119 831, https://doi.org/10.1016/j.atmosenv.2023.119831, 2023.

Park, S.-Y., Dash, U. K., Yu, J., Yumimoto, K., Uno, I., and Song, C. H.: Implementation of an Ensemble Kalman Filter in the Community Multiscale Air Quality Model (CMAQ Model v5.1) for Data Assimilation of Ground-Level $PM_{2.5}$, Geosci. Model Dev., 15, 2773–2790, https://doi.org/10.5194/gmd-15-2773-2022, 2022.

Pérez, C., Nickovic, S., Baldasano, J. M., Sicard, M., Rocadenbosch, F., and Cachorro, V. E.: A Long Saharan Dust Event over the Western Mediterranean: Lidar, Sun Photometer Observations, and Regional Dust Modeling, J. Geophys. Res., 111, D15 214, https://doi.org/10.1029/2005JD006579, 2006.

Pommier, M., Fagerli, H., Schulz, M., Valdebenito, A., Kranenburg, R., and Schaap, M.: Prediction of Source Contributions to Urban Background PM_{10} Concentrations in European Cities: A Case Study for an Episode in December 2016 Using EMEP/MSC-W Rv4.15 and LOTOS-EUROS v2.0 – Part 1: The Country Contributions, Geosci. Model Dev., 13, 1787–1807, https://doi.org/10.5194/gmd-13-1787-2020, 2020.

Rabier, F. and Liu, Z.: Variational Data Assimilation: Theory and Overview, in: Proc. ECMWF Seminar on Recent Developments in Data Assimilation for Atmosphere and Ocean, Reading, UK, September 8–12, pp. 29–43, 2003.

Ravela, S., Emanuel, K., and McLaughlin, D.: Data Assimilation by Field Alignment, Physica D, 230, 127–145, https://doi.org/10.1016/j.physd.2006.09.035, 2007.

Reichle, R. H., McLaughlin, D. B., and Entekhabi, D.: Hydrologic Data Assimilation with the Ensemble Kalman Filter, Mon. Weather Rev., 130, 103–114, https://doi.org/10.1175/1520-0493(2002)130<0103:HDAWTE>2.0.CO;2, 2002.

Shao, Y.: Simplification of a Dust Emission Scheme and Comparison with Data, J. Geophys. Res., 109, D10 202, https://doi.org/10.1029/2003JD004372, 2004.

Shao, Y., Raupach, M., and Leys, J.: A Model for Predicting Aeolian Sand Drift and Dust Entrainment on Scales from Paddock to Region, Soil Res., 34, 309, https://doi.org/10.1071/SR9960309, 1996.

She, L., Xue, Y., Guang, J., Che, Y., Fan, C., Li, Y., and Xie, Y.: Towards a Comprehensive View of Dust Events from Multiple Satellite and Ground Measurements: Exemplified by the May 2017 East Asian Dust Storm, Nat. Hazards Earth Syst. Sci., 18, 3187–3201, https://doi.org/10.5194/nhess-18-3187-2018, 2018.

Skoulidou, I., Koukouli, M.-E., Manders, A., Segers, A., Karagkiozidis, D., Gratsea, M., Balis, D., Bais, A., Gerasopoulos, E., Stavrakou, T., van Geffen, J., Eskes, H., and Richter, A.: Evaluation of the LOTOS-EUROS NO_2 Simulations Using Ground-Based Measurements and S5P/TROPOMI Observations over Greece, Atmos. Chem. Phys., 21, 5269–5288, https://doi.org/10.5194/acp-21-5269-2021, 2021.

Song, L., Bi, X., Zhang, Z., Li, L., Dai, Q., Zhang, W., Li, H., Wang, X., Liang, D., and Feng, Y.: Impact of Sand and Dust Storms on the Atmospheric Environment and Its Source in Tianjin-China, Sci. Total Environ., 825, 153 980, https://doi.org/10.1016/j.scitotenv.2022.153980, 2022.

Tang, W., Dai, T., Cheng, Y., Wang, S., and Liu, Y.: A Study of a Severe Spring Dust Event in 2021 over East Asia with WRF-Chem and Multiple Platforms of Observations, Remote Sens., 14, 3795, https://doi.org/10.3390/rs14153795, 2022.

Timmermans, R., Kranenburg, R., Manders, A., Hendriks, C., Segers, A., Dammers, E., Zhang, Q., Wang, L., Liu, Z., Zeng, L., Denier van der Gon, H., and Schaap, M.: Source Apportionment of $PM_{2.5}$ across China Using LOTOS-EUROS, Atmos. Environ., 164, 370–386, https://doi.org/10.1016/j.atmosenv.2017.06.003, 2017.

TNO: Source Code and User Guidance of LOTOS-EUROS, TNO, last access: August 2023.

Wang, X.: Historical data on air quality in china, https://quotsoft.net/air/, last access: Nov. 2023.

Wu, X., Vu, T. V., Shi, Z., Harrison, R. M., Liu, D., and Cen, K.: Characterization and Source Apportionment of Carbonaceous $PM_{2.5}$ Particles in China - A Review, Atmos. Environ., 189, 187–212, https://doi.org/10.1016/j.atmosenv.2018.06.025, 2018.

Xu, Q., Wei, L., Lu, H., Qiu, C., and Zhao, Q.: Time-Expanded Sampling for Ensemble-Based Filters: Assimilation Experiments with a Shallow-Water Equation Model, J. Geophys. Res., 113, https://doi.org/10.1029/2007JD008624, 2008.

Yarce Botero, A., Lopez-Restrepo, S., Pinel Peláez, N., Quintero, O. L., Segers, A., and Heemink, A. W.: Estimating NOx LOTOS-EUROS CTM Emission Parameters over the Northwest of South America through 4DEnVar TROPOMI NO2 Assimilation, Atmosphere-Basel, 12, 1633, https://doi.org/10.3390/atmos12121633, 2021.

Yumimoto, K. and Takemura, T.: Long-Term Inverse Modeling of Asian Dust: Interannual Variations of Its Emission, Transport, Deposition, and Radiative Forcing, J. Geophys. Res. Atmos., 120, 1582–1607, https://doi.org/10.1002/2014JD022390, 2015.

Zender, C. S., Bian, H., and Newman, D.: Mineral Dust Entrainment and Deposition (DEAD) Model: Description and 1990s Dust Climatology, J. Geophys. Res., 108, https://doi.org/10.1029/2002JD002775, 2003.

Zhang, R., Arimoto, R., An, J., Yabuki, S., and Sun, J.: Ground Observations of a Strong Dust Storm in Beijing in March 2002, J. Geophys. Res., 110, https://doi.org/10.1029/2004JD004589, 2005.

Zhang, X., Sharratt, B., Liu, L., Wang, Z., Pan, X., Lei, J., Wu, S., Huang, S., Guo, Y., Li, J., Tang, X., Yang, T., Tian, Y., Chen, X., Hao, J., Zheng, H., Yang, Y., and Lyu, Y.: East Asian Dust Storm in May 2017: Observations, Modelling, and Its Influence on the Asia-Pacific Region, Atmos. Chem. Phys., 18, 8353–8371, https://doi.org/10.5194/acp-18-8353-2018, 2018.

Zhao, Q., Xu, Q., Jin, Y., McLay, J., and Reynolds, C.: Time-Expanded Sampling for Ensemble-Based Data Assimilation Applied to Conventional and Satellite Observations, Weather Forecasting, 30, 855–872, https://doi.org/10.1175/WAF-D-14-00108.1, 2015.